Advanced Composites and Hybrid Materials (2025) 8:429
https://doi.org/10.1007/s42114-025-01517-5

RESEARCH

Hydrogel-induced ANF-MXene-PEDOT:PSS film by ultra-fast protonation for electromagnetic interference shielding

Shanshan Ma[1,2,3] · Siqi Liu[2] · Jifeng Yan[1] · Bin Ren[1] · Hang Yu[1] · Zhaoyang Ma[4] · Lina Sun[1] · Tengyang Zhang[1] · Jinpeng Huo[5] · Yuhui Yang[3] · Jie Fei[1] · Sanghoon Chae[3] · Chaobin He[2] · Hejun Li[1]

Received: 31 May 2025 / Revised: 15 October 2025 / Accepted: 22 October 2025

Abstract

The development of a multifunctional conductive film to meet the requirements of flexibility, high-strength and exceptional electromagnetic interference (EMI) shielding capacity in the electronic devices has attracted extensive attention. A strategy of hydrogel-induced ultra-fast protonation was proposed for preparing aramid nanofibers-transition metal carbonitrides-poly(3,4-ethylenedioxythiophene):poly(styrene sulfonate) (ANF-MXene-PEDOT:PSS) conductive films. The ultra-fast protonation process would induce the formation of ultra-long molecular chains and the reconstruction of cross-linking networks to enhance the mechanical properties of films. The ultimate tensile strength of ANF-MXene-PEDOT:PSS (60%) film reached 233.6 MPa, showing an increase of 189.5%. Meanwhile, the encapsulation of conductive PEDOT:PSS layer effectively addressed the issues of the brittleness and highly oxidization susceptibility of MXene. The EMI shielding effectiveness of ANF-MXene-PEDOT:PSS (60%) film reached 45.7–48.2 dB from 8.2 to 26.7 GHz at a thickness of 36 μm. After a month for exposing to air, the EMI shielding capability of ANF-MXene-PEDOT:PSS (60%) film still remained stable (> 42.5 dB). This hybrid film also exhibited high conductivity (264.7 S·cm^{-1}), self-cleaning, fire retardancy and joule heating properties, which was as an intelligent sensor to realize the real-time monitoring of human physiological signals. This work paves the way for large-scale production of next-generation high-performance EMI shielding films, demonstrating huge potential in electromagnetic protection, thermal management and intelligent wearable devices.

Keywords ANF-MXene-PEDOT:PSS film · Ultra-fast protonation · Electromagnetic interference shielding · Joule heating · Intelligent sensing

1 Introduction

With the wide-spread use of electronic devices, electromagnetic pollution has gradually become an urgent challenge in the aerospace, military and engineering fields [1]. Therefore, developing high-performance electromagnetic interference (EMI) shielding materials has attracted huge attention. The explosive growth of electronic devices consumption proposed higher demands including flexibility, high strength, light-weight, ultra-thin and excellent EMI shielding performances for next-generation of EMI shielding materials [2]. Recently, conductive nanomaterials including graphene

---

✉ Jie Fei
feijiecc@nwpu.edu.cn

✉ Sanghoon Chae
sanghoon.chae@ntu.edu.sg

✉ Chaobin He
msehc@nus.edu.sg

✉ Hejun Li
lihejun@nwpu.edu.cn

[1] State Key Laboratory of Solidification Processing, School of Materials Science and Engineering, Northwestern Polytechnical University, Xi'an 710072, China

[2] Department of Materials Science & Engineering, National University of Singapore, 9 Engineering Drive 1, Singapore 117574, Singapore

[3] School of Electrical and Electronic Engineering, Nanyang Technological University, 50 Nanyang Avenue, Singapore 639798, Singapore

[4] Sinosteel Group Luoyang Refractories Research Institute Co., Ltd, Luoyang 471000, China

[5] State Key Laboratory of Clean and Efficient Turbomachinery Power Equipment, Department of Mechanical Engineering, Tsinghua University, Beijing 100084, China

[3], silver nanowires [4], carbon nanotubes (CNTs) [5] and transition metal carbonitrides (MXene) [2] displayed significant advantages for prepare EMI shielding materials, owing to high conductivity, low density and easy processability. Among above conductive fillers, MXene as a kind of newly emerging two-dimensional (2D) nanosheets, gained great attention for its remarkable electrical conductivity and lamellar structure. Unique laminated structure and metallic conductive nature of MXene was conducive to multiple reflections and rapid attenuation of electromagnetic waves [6]. Shahzad and coworkers [6] demonstrated that the EMI shielding capacity of MXene film could reach 92 dB for blocking 99.99999994% radiation. It was obvious that MXene exhibited great potential in preparing light-weight EMI shielding film for new-generation electronic devices. However, the weak interaction between MXene nanosheets resulted in the poor strength of pure MXene film. Air sensitivity and highly oxidization susceptibility further limited the large-scale production of MXene film [7].

Considering abundant active groups on the surface of MXene, the introduction of macromolecular polymers including cellulose nanofiber (CNF) [8, 9], aramid nanofiber (ANF) [10, 11] and polyvinyl alcohol (PVA) [12] was a direct and effective strategy to strengthen interlayer interactions of MXene nanosheets. Chen and coworkers [2] reported that the MXene/CNF composite film exhibited a tensile strength and EMI SE of 135.4 MPa and 25.8 dB based on the method of vacuum filtration. ANF has become a noticeable candidate to construct flexible and high-strength composite films in terms of outstanding mechanical properties and high temperature stability [11], which acted as an efficient glue to reinforce the bonding forces between nanosheets. The resulting 80%MXene/20%ANF composites demonstrated that the EMI shielding value and tensile strength reached 40.6 dB and 92.0 MPa, while the EMI shielding effectiveness of 40%MXene/60%ANF composites reduced to 28.1 dB, when the strength was 201.3 MPa [13]. The above results indicated that the existence of one-dimensional (1D) nanofibers was beneficial to promoting the strength of films. Nevertheless, it was difficult to simultaneously meet the requirements of high strength and prominent EMI shielding performance by a simple vacuum filtration of nanofibers/MXene.

In this work, we proposed a strategy of hydrogel-induced ultra-fast protonation to manufacture multifunctional aramid nanofiber-transition metal carbonitride-poly(3,4-ethyl enedioxythiophene):poly(styrene sulfonate) (ANF-MXene-PEDOT:PSS) conductive films. Adopting PVA hydrogel as a substrate effectively facilitated the in-situ phase separation and instantaneously provided large quantities of proton donors, further inducing the construction of high-density hydrogen bonding networks and the formation of ANF hydrogel film. The above high-density hydrogen bonding networks guaranteed the structural stability and enhanced the mechanical strength of films. Notably, the incorporation of MXene and PEDOT:PSS significantly promoted the electrical conductivity and EMI shielding capability of hybrid films. Meanwhile, the encapsulation of conductive PEDOT:PSS layer effectively mitigated rapid oxidation of MXene to maintain high EMI shielding capability of films. According to hydrogel-induced ultra-fast protonation process, 1D ANF, 2D MXene and 1D PEDOT:PSS as functional building blocks, were assembled to construct a flexible and mechanically strong hybrid film with a gradient laminar structure, which was conducive to the multiple internal reflections to dissipate the energy of electromagnetic waves. This work provided a direct and efficient method for assembling nanoscale building blocks to construct advanced EMI shielding films, indicating a promising potential in wearable electromagnetic protection, aerospace and green electronics.

2 Experimental section

2.1 Materials

Aramid fibers (length, 1 cm) and Ti_3AlC_2 powder (particle size, 500 mesh) were purchased by DuPont and Yejin 79 Technology Co., Ltd. Hydrochloric acid (HCl, 36.0–38.0 *wt.*%), dimethyl sulfoxide (DMSO, 99%) and sulfuric acid (H_2SO_4, 98%) were obtained from Tianjin Damao Chemical Co., Ltd. Lithium fluoride (LiF, 99%), polyvinyl alcohol (PVA, molecular weight, 146,000–186,000) and potassium hydroxide (KOH, 90%) were acquired by Aladdin Industrial Co., Ltd. PEDOT: PSS dispersion (concentration, 1.5 *wt.*%; viscosity, 55 mPa·s; color, dark blue) was provided by Shanghai Ouyi Organic Photoelectric Material Technology Co., Ltd. The above chemical reagents were employed in the experiment without further purification.

2.2 Sample preparation

2.2.1 Preparation of ANF/DMSO and MXene/H_2O dispersion

Aramid fibers (4 g) and KOH (6.0 g) were placed into the flask with 200 mL DMSO and 8 mL deionized water for 5 h with continuous magnetic stirring at 50 °C [14–17]. When the above solution became transparent and dark red, the ANF/DMSO dispersion was obtained. As reported in the literatures [18, 19], MXene/H_2O dispersion was acquired by acid etching, ultrasonic dispersion and repeated centrifugation processes. Firstly, LiF (3.0 g) was placed into a Teflon reaction tank with 60 mL HCl (9 mol/L) under the assistance of magnetic stirring at ambient temperature for 30 min. Subsequently, 3.0 g Ti_3AlC_2 was added into the tank with continuous magnetic stirring for 36 h at 35 ℃ to remove Al layer. After etching, the above reaction products were transferred into centrifuge tubes to centrifugate (3500 rpm, 5 min) and wash with deionized water for 6–8 times until the pH of the dispersion reached 6. The etched sediment was collected for ultrasonic dispersion treatment at 4 ℃ for 30 min to achieve the exfoliation of multilayered $Ti_3C_2T_x$. Later, the above dispersion was centrifuged for 10 min at 6000 rpm. Until the color of centrifuged supernatant became light green, $Ti_3C_2T_x/H_2O$ dispersion was acquired by repeating the above process.

2.2.2 Construction of PVA hydrogel

In this experiment, the PVA hydrogel as an effective reaction substrate was prepared by freeze–thaw and solvent exchange processes [20, 21]. 20 g of PVA was added into the beaker with 64 g DMSO and 16 g deionized water at 140 °C for 2.5 h, under the condition of continuous stirring (400 rpm). After swelling and completely dissolving, the above hydrogel precursor was transferred into the mold and kept in the freezer at −18 ℃ for 12 h. Then the sample was thawed at room temperature for 2 h and the process was repeated for three times to enhance cross-linking networks of the hydrogel. After finishing, the above hydrogel was placed the Petri dish with deionized water for 4 days to achieve solvent exchange.

2.2.3 Fabrication of ANF-MXene-PEDOT:PSS film

The fabrication of ANF-MXene-PEDOT:PSS hybrid film included the preparation of PVA hydrogel, rapid formation of ANF hydrogel film, multiple vacuum filtration, hot-pressing and acid impregnation processes. The prepared ANF/DMSO dispersion was evenly dropped on the surface of PVA hydrogel. Due to the high moisture content of PVA hydrogel, the reaction solution would extend rapidly on the surface of hydrogel. Meanwhile, the DMSO in ANF/DMSO dispersion would rapidly diffuse from the surface of liquid film to the interior of hydrogel. After in-situ phase separation of DMSO, the above process induced rapid cross-linking of hydrogen bonds to form a hydrogel film on the surface of PVA hydrogel. Subsequently, the above hydrogel film was stripped from the hydrogel surface and transferred into a deionized water bath. After 1 h drying at room temperature, ANF film was obtained by hot-pressing treatment (60 ℃, 5 MPa, 2 h). For ANF-MXene film, it was achieved by the vacuum filtration with the $MXene/H_2O$ and similar drying process. A series of ANF-MXene-PEDOT:PSS films with MXene-PEDOT:PSS loading (the weight ratio of MXene and PEDOT:PSS was 1:1) of 40, 50, 60 *wt.%* were obtained. To enhance electrical conductivity, ANF-MXene-PEDOT:PSS (40%), (50%), (60%) films were immersed in dilute H_2SO_4 solution (1 M) for 30 min at room temperature. After immersing, it was washed with deionized water for three times and dried.

2.3 Characteristic analysis

The morphologies of ANF, MXene and PEDOT:PSS were characterized by a SEM (Verios G4, FEI, USA) and TEM (Talos F200X, FEI, USA). Meanwhile, surface morphologies and elemental analysis of ANF, ANF-MXene and ANF-MXene-PEDOT:PSS films were observed by a SEM (VEGA-3-SBH, Tescan, Czech) with an EDS (Inca X-MAX, Oxford, US). XRD spectra and crystallinity of ANF, MXene and hybrid films were characterized by a D8 Advance (Bruker, Germany) from 5° to 60°, at 40 kV and 20 mA. The X-ray photoelectron spectroscopy (XPS, Kratos, Japan) was employed to characterize the chemical states of samples. The thermal stability of ANF, MXene and ANF-MXene-PEDOT:PSS (60%) film was detected by a thermal analyzer (STA449F3, NETZSCH, Germany) from 25 to 800 °C at N_2. Tensile strength of various films was characterized by a universal testing instrument (CMT5304, Shenzhen SANS, China) with the loading rate of 0.5 mm/min. Surface temperature and infrared images of hybrid films were detected by an infrared camera (T3Pro, IRay, China). The contact angle testing of samples was conducted by an optical contact angle meter (OCA20, Dataphysics, Germany). According to the statistics of 100 fibers, the diameter distribution of ANF was analyzed by the software of Image J. Water vapor permeability was measured by a water method in ASTM E96-95 [22]. ANF, ANF-MXene and ANF-MXene-PEDOT:PSS (60%) films were sealed around the rim of the bottle containing water. The above bottle was kept at 23 ± 1 °C, $50 \pm 2\%$ RH and the weight of bottle was recorded for 7 days to obtain an average value.

The electrical conductivity of samples was detected by a Hall effect testing equipment (ET9105-HS, Beijing Hifuta Technology Co., China) according to the standard four-point contact strategy [23, 24]. Moreover, EMI shielding performances of different films were characterized by a vector network analyzer (E8362E, Anritsu Communication Technology (Shanghai) Co., China) during the 8.2–12.4 GHz (X-band), 12.4–18.0 GHz (Ku-band) and 18.0–26.6 GHz (K-band) according to a waveguide method. Related coefficients of reflection (R), absorption (A) and transmission (T) were calculated from the data of S11 and S21 as shown in Eqs. 1, 2 and 3 [19]. Meanwhile, the SE of T, R, A and multiple internal reflections (SE_M) of samples could be acquired by Eqs. 4, 5 and 6 [19]. Additionally, the SE_M could be ignored, when the SE_T exceeded 15 dB [18]. To accurately evaluate the EMI shielding capability of hybrid films, the shielding effectiveness per thickness (SSE_t) of films could be obtained by Eq. 7 [6, 18, 25].

$$R = 10^{(\frac{S_{11}}{10})} \tag{1}$$

$$T = 10^{\sim\imath^{,}\frac{S_{21}}{10}\sim\imath^{\circ}} \tag{2}$$

$$A=1-R-T \tag{3}$$

$$SE_T = SE_R + SE_A + SE_M \tag{4}$$

$$SE_R = -10\ 1og(1 - R) \tag{5}$$

$$SE_A = -10\ 1og\left(\frac{T}{1 - R}\right) \tag{6}$$

$$SSE_t = \frac{SE_T}{\rho t} \tag{7}$$

where ρ and t represented the density and thickness of hybrid film. Five groups of parallel experiments were conducted to acquire an average value.

Related sensing experiments of ANF-MXene-PEDOT:PSS (60%) film were carried out by the electrochemical workstation (CHI600E, Shenzhen Junda Times Instrument Co., China). The hybrid film (1×1 cm^2) was sandwiched between the fork finger electrode material and tape for assembling as a smart sensor to connect with the chemical workstation using copper tape and wire. The above sensor could be adhered on the finger and wrist to collect physiological signals and monitor health status of human.

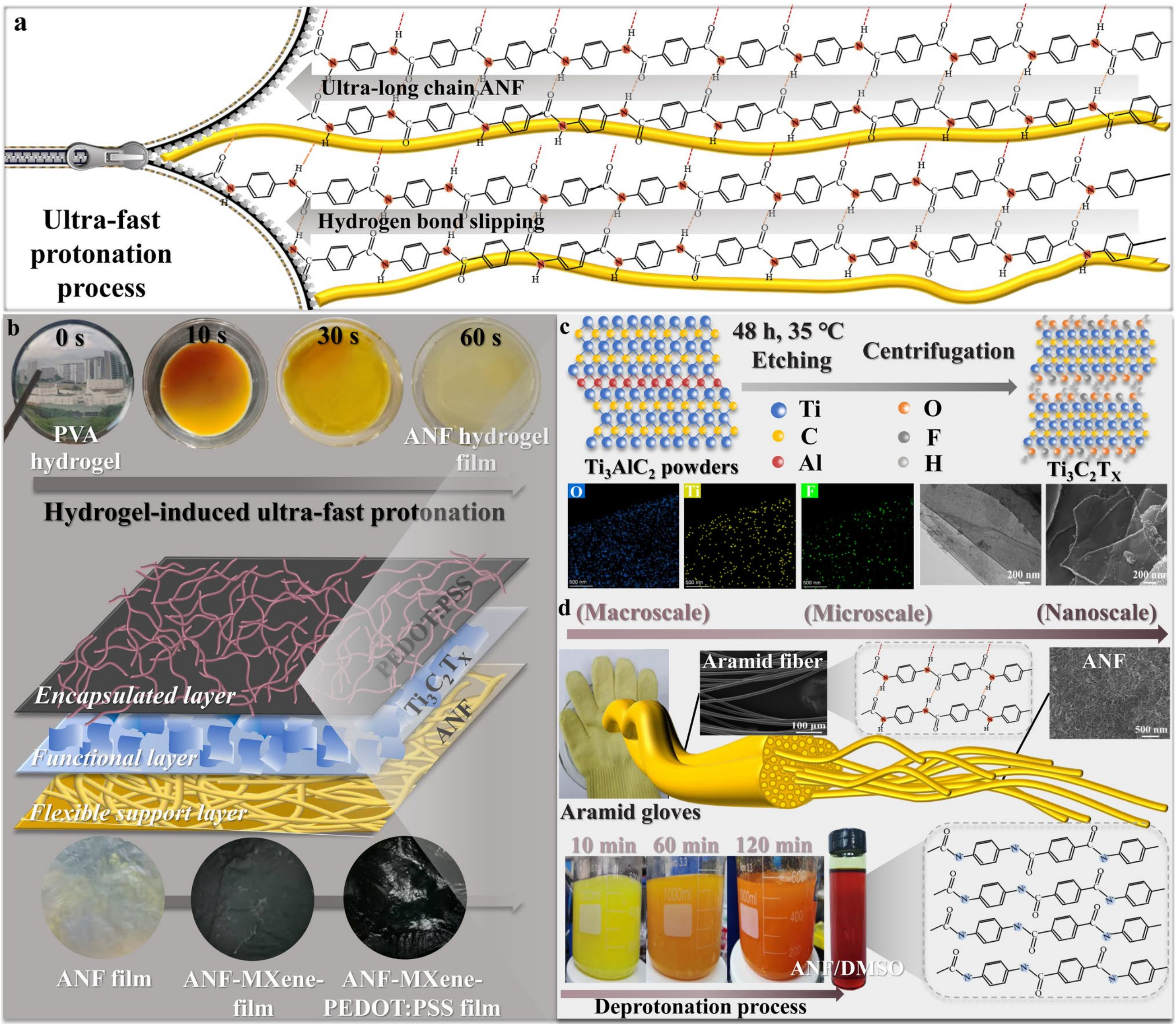

Fig. 1 Ultra-fast protonation process and preparation of ANF-MXene-PEDOT:PSS film. **a** Schematic diagram of ultra-fast protonation process; **(b)** Structural diagram of ANF-MXene-PEDOT:PSS film; **(c-d)** Preparation process of $Ti_3C_2T_x$ nanosheets and ANF

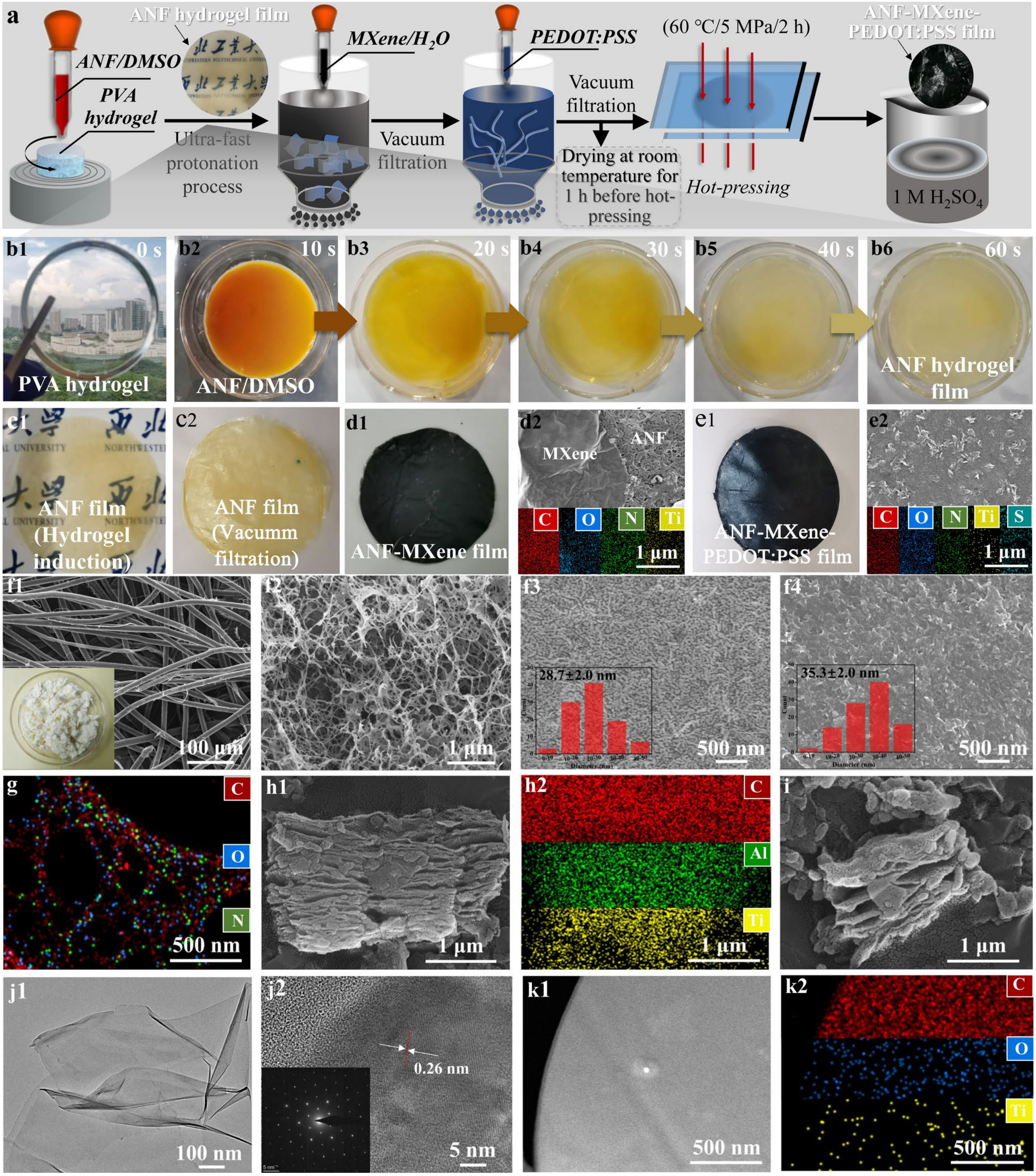

Fig. 2 Preparation process of ANF-MXene-PEDOT:PSS film and surface morphologies of aramid fiber, ANF film (hydrogel induction), ANF film (vacuum filtration), Ti_3AlC_2 powder, multilayered $Ti_3C_2T_x$ and MXene nanosheets. **a** Schematic illustration of preparing ANF-MXene-PEDOT:PSS film. **(b1-b6)** Ultra-fast protonation process for forming ANF hydrogel film; Digital photograph of **(c1)** ANF film (hydrogel induction), **(c2)** ANF film (vacuum filtration), **(d1)** ANF-MXene film and **(e1)** ANF-MXene-PEDOT:PSS (60%) film; SEM images of **(d2)** ANF-MXene film, **(e2)** ANF-MXene-PEDOT:PSS (60%) film, **(f1)** aramid fiber, **(f2)** ANF, **(f3)** ANF film (hydrogel induction) and **(f4)** ANF film (vacuum filtration); Element mapping images of **(g)** ANF and **(h2)** Ti_3AlC_2; SEM images of **(h1)** Ti_3AlC_2 powder and **(i)** multilayered $Ti_3C_2T_x$; **(j1-j2)** TEM and HRTEM images of MXene; **(k1-k2)** SEM and element mapping images of MXene

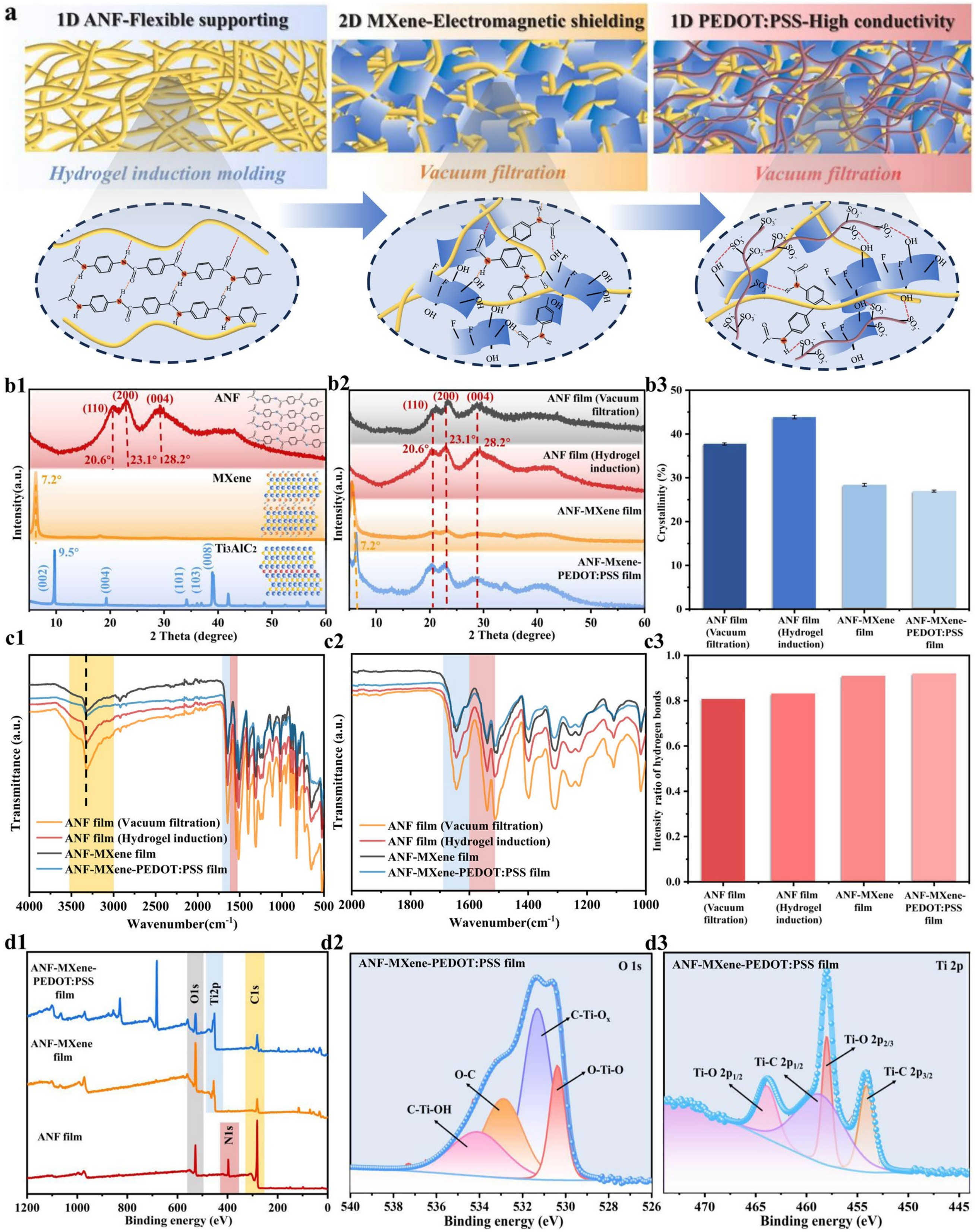
a
1D ANF-Flexible supporting
2D MXene-Electromagnetic shielding
1D PEDOT:PSS-High conductivity
Hydrogel induction molding
Vacuum filtration
Vacuum filtration
OH
F
SO_3^-
b1
(110)
(200)
(004)
ANF
20.6°
23.1°
28.2°
MXene
7.2°
Ti_3AlC_2
9.5°
(002)
(004)
(101)
(103)
(008)
Intensity(a.u.)
2 Theta (degree)
b2
ANF film (Vacuum filtration)
ANF film (Hydrogel induction)
ANF-MXene film
ANF-Mxene-PEDOT:PSS film
b3
Crystallinity (%)
ANF film (Vacuum filtration)
ANF film (Hydrogel induction)
ANF-MXene film
ANF-MXene-PEDOT:PSS film
c1
Transmittance (a.u.)
Wavenumber(cm^{-1})
ANF film (Vacuum filtration)
ANF film (Hydrogel induction)
ANF-MXene film
ANF-MXene-PEDOT:PSS film
c2
c3
Intensity ratio of hydrogen bonds
d1
ANF-MXene-PEDOT:PSS film
ANF-MXene film
ANF film
O1s
Ti2p
C1s
N1s
Binding energy (eV)
d2
ANF-MXene-PEDOT:PSS film
O 1s
C-Ti-O_x
O-Ti-O
O-C
C-Ti-OH
d3
Ti 2p
Ti-O $2p_{1/2}$
Ti-C $2p_{1/2}$
Ti-O $2p_{2/3}$
Ti-C $2p_{3/2}$

◂**Fig. 3** Skeleton construction of ANF-MXene-PEDOT:PSS film and surface chemistry analysis of samples. **a** Skeleton construction of ANF-MXene-PEDOT:PSS film; **(b1-b3)** XRD patterns and crystallinity analysis of samples; **(c1-c3)** FTIR spectrum of various films and intensity ratio of hydrogen bonds; **(d1-d3)** XPS spectra and analysis of ANF, ANF-MXene and ANF-MXene-PEDOT:PSS (60%) films

3 Results and discussion

3.1 Hydrogel-induced ANF-MXene-PEDOT:PSS film

There were several preconditions to obtain a flexible film with excellent mechanical strength and EMI shielding capacity: (1) constructing strong interfacial interactions was necessary and (2) highly conductive networks were responsible for exceptional EMI shielding performances. To meet above conditions simultaneously, 1D ANF, 2D MXene nanosheets and 1D PEDOT:PSS as functional building blocks were utilized for the scale-up production of high-performance hybrid film (Fig. 1a-b).

As displayed in Fig. 1c, MXene nanosheets were acquired by selectively etching Al atoms from Ti_3AlC_2 powder and ultrasound dispersion of multilayered $Ti_3C_2T_x$. The transformation from macroscopic fibers to aramid nanofibers could be accomplished by a top-down strategy [10, 16, 26–30] (Fig. 1d). In this work, transparent PVA hydrogel as a template could effectively promote the ultra-fast protonation and the formation of ANF hydrogel film. The high moisture content of PVA hydrogel was beneficial for providing a large number of proton donors to facilitate the ultra-fast reconstruction of hydrogen bonding between molecular chains. During in-situ phase separation process, proton donors rapidly diffused from the interior of PVA hydrogel to the surface of ANF liquid film. Compared with the vacuum filtration of ANF/H_2O [15, 31], the above strategy was more

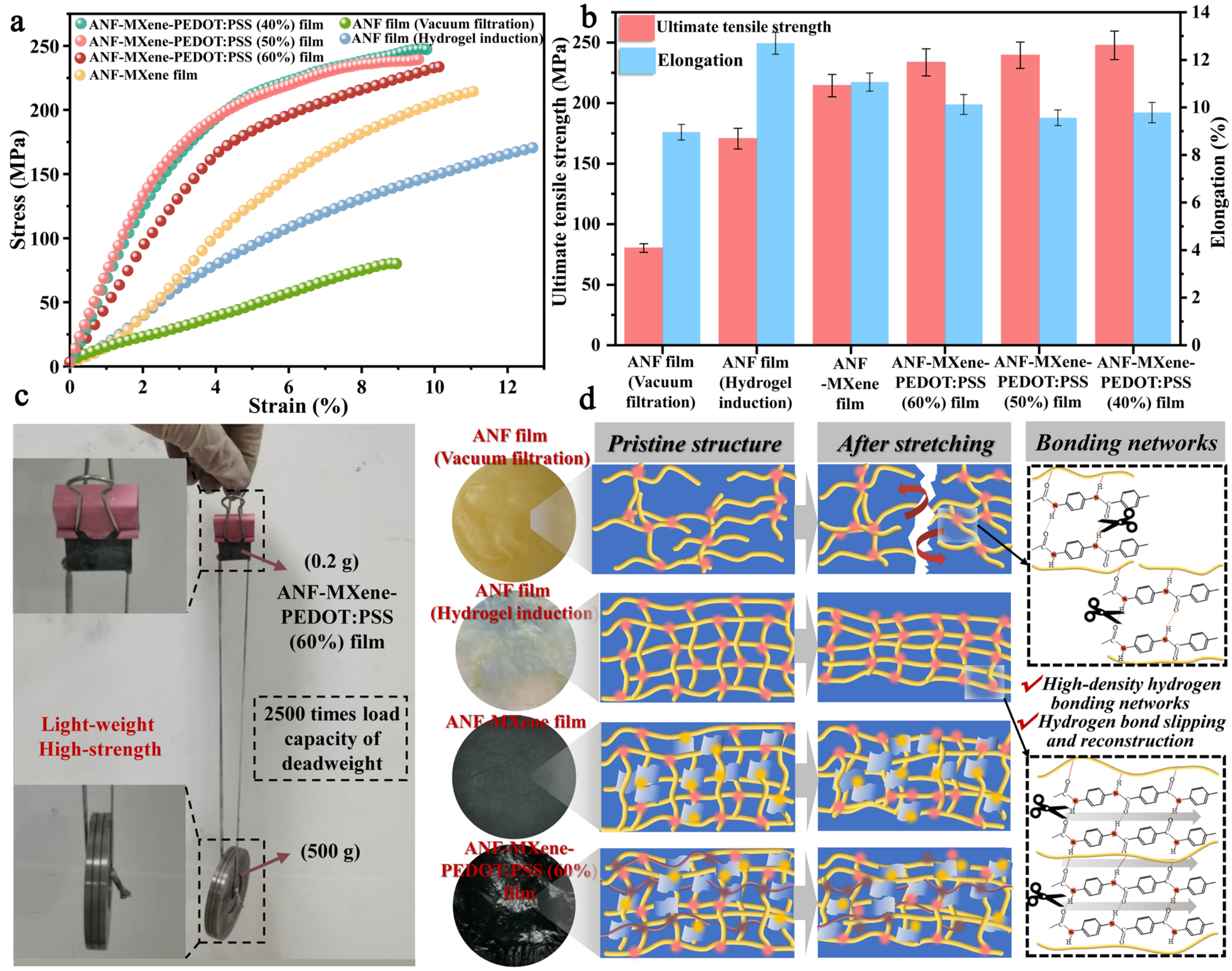

Fig. 4 Stress–strain curves and tensile strength of ANF, ANF-MXene and ANF-MXene-PEDOT:PSS (40%), (50%), (60%) films**. a-b** Related stress–strain curves and tensile strength of samples; **(c)** The ANF-MXene-PEDOT:PSS (60%) film (0.2 g) holding 500 g standard weight; **(d)** Different tensile fracture mechanism of ANF, ANF-MXene and ANF-MXene-PEDOT:PSS (60%) films

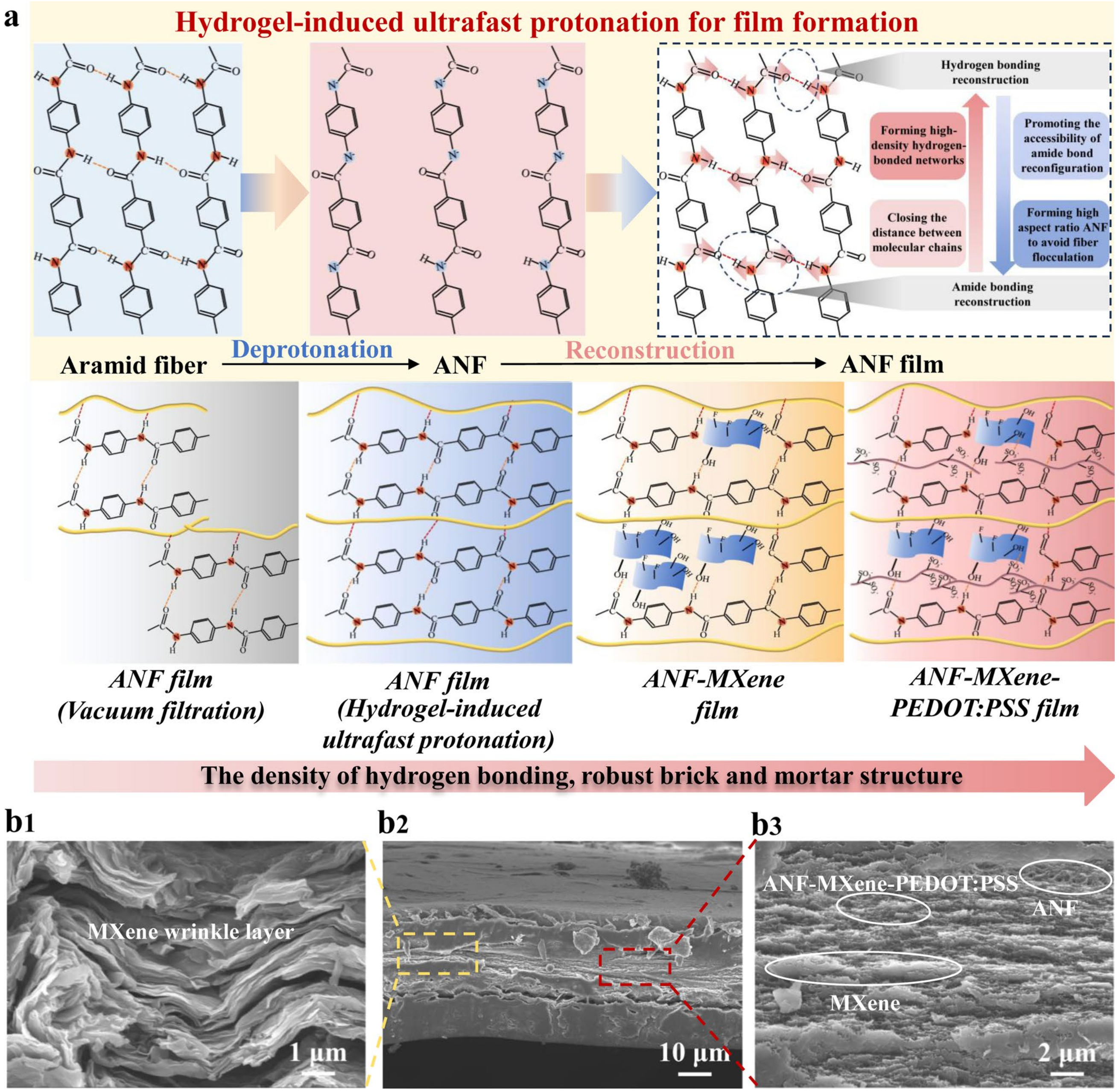

Fig. 5 Schematic diagram of the interlayer bonding mechanism and cross-sectional morphologies of ANF-MXene-PEDOT:PSS (60%) film. **a** Diagram of the interlayer bonding mechanism of various films; **(b1-b3)** SEM images of MXene layer in ANF-MXene-PEDOT:PSS (60%) film

favorable to the formation of ultra-long molecular chains, further inducing the construction of high-density hydrogen bonding networks between molecular chains. When subjected to external stretching, high-density hydrogen bonding networks guaranteed the structural stability of ANF-MXene-PEDOT:PSS film, thus enhancing the mechanical strength of hybrid film. For ANF-MXene-PEDOT:PSS film, flexible and porous ANF networks facilitated stress buffering and dispersing and the presence of MXene layer could provide a 2D skeleton for resisting to external damage. Meanwhile, the encapsulated layer of highly conductive PEDOT:PSS, was in favor of enhancing the interlayer force and protecting MXene layer from rapid oxidation. Therefore, the resultant multifunctional hybrid film was expected that it would exhibit high-strength, outstanding EMI shielding performance, satisfactory intelligent sensing and joule heating properties.

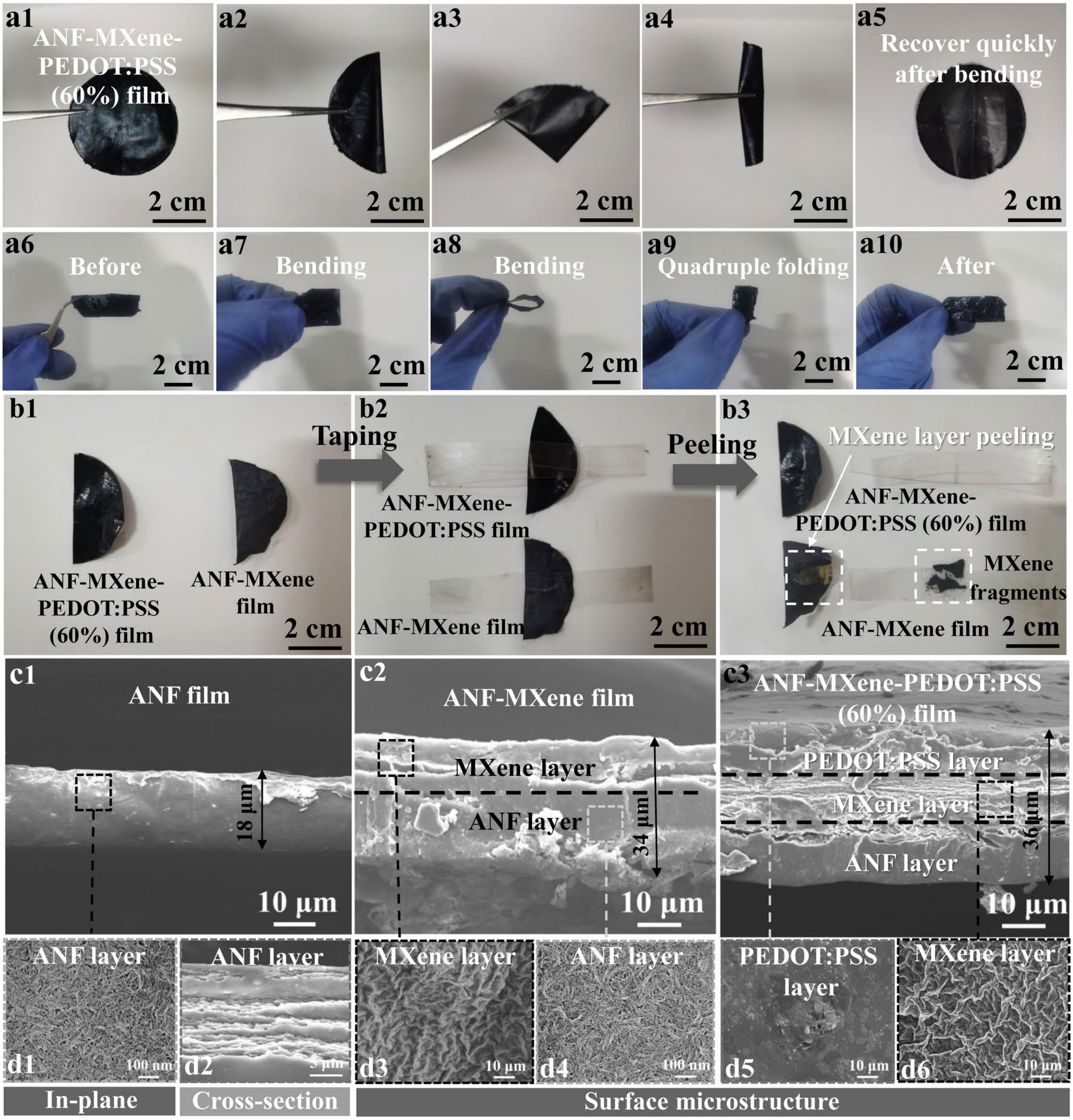

Fig. 6 Digital photograph and surface morphology of various films. **a1** Digital photograph of ANF-MXene-PEDOT:PSS (60%) film; **(a2-a10)** Folding and crimping of flexible hybrid film; **(b1-b3)** Tape peeling experiment for the adhesion of hybrid films; **(c1-c3)** Cross-section morphologies of ANF, ANF-MXene and ANF-MXene-PEDOT:PSS (60%) films; **(d1-d6)** Surface microstructure of ANF, MXene and PEDOT:PSS layers in the films

Figure 2a-b illustrated the preparation process of ANF-MXene-PEDOT:PSS film by an ultra-fast protonation method. It was obvious that the abundant proton donors on the surface of PVA hydrogel induced the ultra-fast formation of ANF hydrogel film in 60 s (Fig. 2b1-6). Digital photographs and surface morphologies of ANF film (hydrogel induction), ANF film (vacuum filtration), ANF-MXene film and ANF-MXene-PEDOT:PSS (60%) film were shown in Fig. 2c1-e2. Moreover, surface morphologies and element mapping images of aramid fiber, ANF, Ti_3AlC_2 powder, multilayered $Ti_3C_2T_x$ and MXene nanosheets were exhibited in Fig. 2f1-k2. Macroscopic aramid fibers gradually

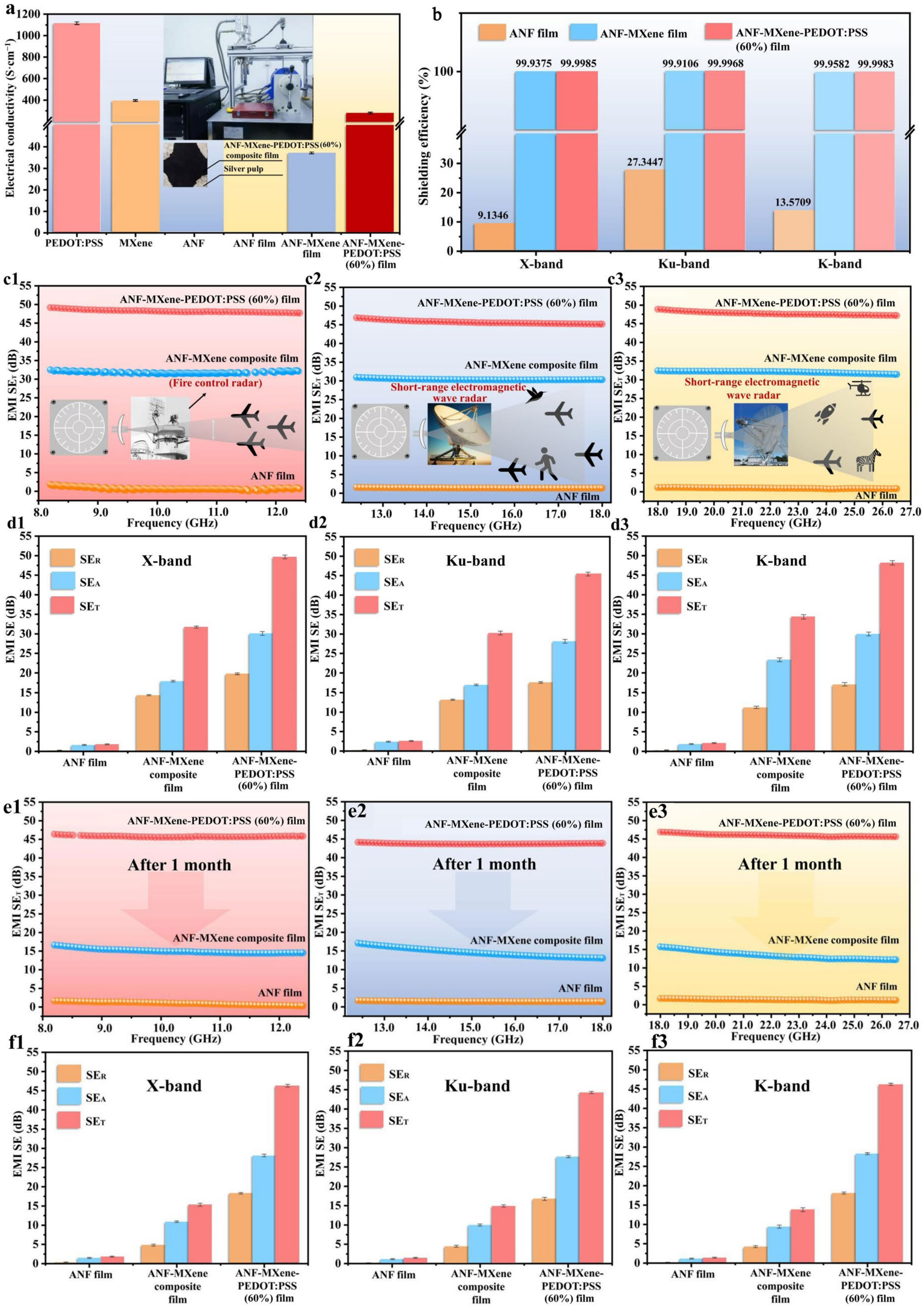
a
Electrical conductivity (S·cm⁻¹)
1200
1000
800
600
400
40
30
20
10
0
ANF-MXene-PEDOT:PSS(60%) composite film
Silver pulp
PEDOT:PSS
MXene
ANF
ANF film
ANF-MXene film
ANF-MXene-PEDOT:PSS (60%) film
b
ANF film
ANF-MXene film
ANF-MXene-PEDOT:PSS (60%) film
Shielding efficiency (%)
100
30
20
10
0
99.9375
99.9985
99.9106
99.9968
99.9582
99.9983
9.1346
27.3447
13.5709
X-band
Ku-band
K-band
c1
EMI SET (dB)
ANF-MXene-PEDOT:PSS (60%) film
ANF-MXene composite film
(Fire control radar)
ANF film
8.0
9.0
10.0
11.0
12.0
Frequency (GHz)
c2
ANF-MXene-PEDOT:PSS (60%) film
ANF-MXene composite film
Short-range electromagnetic wave radar
ANF film
13.0
14.0
15.0
16.0
17.0
18.0
Frequency (GHz)
c3
ANF-MXene-PEDOT:PSS (60%) film
ANF-MXene composite film
Short-range electromagnetic wave radar
ANF film
18.0
19.0
20.0
21.0
22.0
23.0
24.0
25.0
26.0
27.0
Frequency (GHz)
d1
EMI SE (dB)
SER
SEA
SET
X-band
ANF film
ANF-MXene composite film
ANF-MXene-PEDOT:PSS (60%) film
d2
Ku-band
d3
K-band
e1
EMI SET (dB)
ANF-MXene-PEDOT:PSS (60%) film
After 1 month
ANF-MXene composite film
ANF film
Frequency (GHz)
e2
After 1 month
e3
After 1 month
f1
X-band
f2
Ku-band
f3
K-band
55
50
45
40
35
30
25
20
15
10
5
0

◂**Fig. 7** EMI shielding performances of ANF, ANF-MXene and ANF-MXene-PEDOT:PSS (60%) films**. a** Electrical conductivity of PEDOT:PSS, MXene, ANF, ANF film, ANF-MXene film and ANF-MXene-PEDOT:PSS (60%) film; **(b)** Shielding efficiency of different films; **(c-d)** SE_R, SE_A, SE_T of various films in X-band, Ku-band and K-band; **(e–f)** SE_R, SE_A and SE_T of various films in X-band, Ku-band and K-band after one month

transformed into high aspect ratio nanofibrils under the strong alkali effect of KOH/DMSO [16, 29, 30] (Fig. 2f1-2). It could be observed from Fig. 2f3-4 that the average diameter of the ANFs reached 28.7 ± 2.0 nm and 35.3 ± 2.0 nm after hydrogel induction and vacuum filtration. The ANF with a smaller diameter in hydrogel-induced film was contributed to forming denser molecular chain entanglements and crosslinking networks. Detailed elemental mapping image of ANF was shown in Fig. 2g. The existence of above nanofibers was in favor of alleviating the serious flocculation of MXene nanosheets, further facilitating the construction of a robust brick–mortar structure at the interface. Meanwhile, it also could be observed from XRD curves (Fig. 3b1-b2) that the diffraction peaks at 19.2° (004), 33.8° (101) and 39.2° (008) gradually disappeared after acid etching and ultrasonic dispersion [32]. Interesting, the typical peak (002) was kept and shifted from 9.5° in Ti_3AlC_2 powder (Fig. 2h1−2) to 7.2° in MXene nanosheets (Fig. 2j1-k2), further indicating the successful etching and stripping of Ti_3AlC_2 powder. As shown in the results of XPS analysis (Fig. 3d1-d3), a typical peak of Ti–O-C (456.9 eV) appeared on the surface of ANF-MXene-PEDOT:PSS (60%) film, compared with MXene nanosheets.

The skeleton construction of ANF-MXene-PEDOT:PSS film was displayed in Fig. 3a. According to a hydrogel-induced ultrafast protonation process, the ultra-long molecular chains of ANF were tightly entangled to form a high-density network structure. 2D MXene nanosheets with strong EMI shielding capability and 1D PEDOT:PSS with high conductivity sequentially deposited on the ANF film with the assistance of vacuum filtration. It could be observed from Fig. 3b3 that the crystallinity of ANF film (hydrogel induction) was higher than that of ANF film (vacuum filtration). The enhancement of hydrogen bonding promoted the ordered arrangement of molecular chains, resulting in the increase of crystalline zones (Fig. 3c3). As exhibited in Fig. 3c1-c2, the peaks spanning from 3000 to 3500 cm^{-1} belonged to the N–H and O–H stretching vibration peaks, which indicated a slight redshift, further illustrating an enhancement of hydrogen bonding. Meanwhile, it could be seen in Fig. 3c3 that the intensity ratio of hydrogen bonds increased from 0.805 (ANF film (vacuum filtration)) to 0.917 (ANF-MXene-PEDOT:PSS (60%) film). The above redshift phenomenon could be explained that the ultra-fast protonation process would induce the rapid reconstruction of hydrogen bonding networks and enhance bonding forces between ANF and MXene. Additionally, the design of PEDOT:PSS layer could not only effectively improve the conductivity of hybrid film, but also avoid the rapid oxidation of MXene layer.

3.2 Mechanical properties of ANF-MXene-PEDOT:PSS film

Oxidization-prone performance and low strength limited the scale-up production of pure MXene film [5, 19]. To overcome the above issues, highly conductive PEDOT:PSS was coated on the surface of MXene layer to form an encapsulated layer for mitigating the rapid oxidation of MXene. Meanwhile, design of gradient layered structure contributed to achieving the effective dispersion of external stress for enhancing mechanical properties and extending service life of hybrid films. Related stress–strain curves, ultimate tensile strength and elongation of ANF, ANF-MXene and ANF-MXene-PEDOT:PSS (40%), (50%), (60%) films were illustrated in Fig. 4a-b. The vacuum filtration of ANF/H_2O was a common strategy to prepare ANF film [31, 33, 34]. The ultimate tensile strength of ANF film was 80.7 MPa based on above method (Fig. 4a). Meanwhile, it could be observed from Fig. 4a that the ultimate tensile strength of ANF film reached 170.6 MPa according to hydrogel induction, showing an increase of 111.4%.

The above results could be explained by the fact that the formation of the ultra-long molecular chains during hydrogel-induced ultra-fast protonation process was beneficial for the entanglement of molecular chains and the construction of hydrogen bonding networks, which further enhanced the strength properties of hybrid film. After the multi-vacuum filtration of MXene and PEDOT:PSS, there was an upward trend in the tensile strength of hybrid films (Fig. 4a). It could be seen in Fig. 4b that the ultimate tensile strength of ANF-MXene film was 214.5 MPa under the elongation of 12.7%. Meanwhile, the ultimate tensile strength of ANF-MXene-PEDOT:PSS (40%), (50%) and (60%) films reached 247.7, 239.6 and 233.6 MPa, displaying a 206.9%, 196.9% and 189.5% increase, respectively. The rising in the ultimate tensile strength could be attributed to the formation of a robust brick–mortar structure on the interface between MXene and ANF layers, which was conducive to improving the transfer efficiency of external stress [35, 36]. As previous literatures reported [37], the tensile strength of ANF/MXene-PEDOT:PSS film was 155.9 MPa based on the method of direct vacuum filtration. Compared with the above strategy, the hydrogel-induced ultra-fast protonation process demonstrated significant advantages in enhancing the strength of film. For ANF-MXene-PEDOT:PSS hybrid film, high-density hydrogen bonding networks and unique brick–mortar structures were responsible for its exceptional tensile strength. It also could be observed from Fig. 4c that

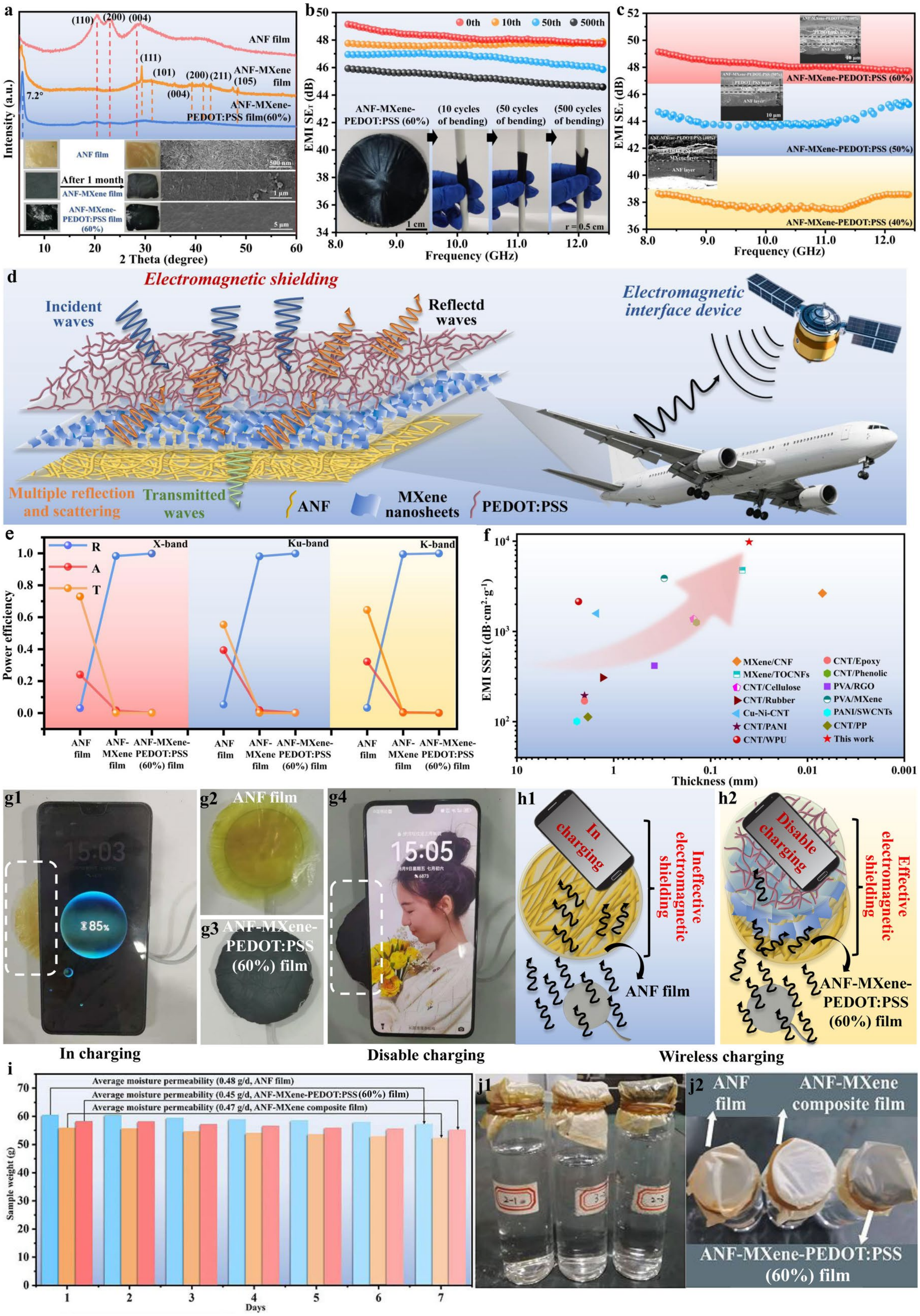
a
(110)
(200)
(004)
ANF film
(111)
(101)
(200)
(211)
(105)
(004)
ANF-MXene film
7.2°
ANF-MXene-PEDOT:PSS film(60%)
Intensity (a.u.)
ANF film
After 1 month
ANF-MXene film
ANF-MXene-PEDOT:PSS film (60%)
500 nm
1 μm
5 μm
2 Theta (degree)
b
0th
10th
50th
500th
EMI SE$_T$ (dB)
ANF-MXene-PEDOT:PSS (60%)
(10 cycles of bending)
(50 cycles of bending)
(500 cycles of bending)
1 cm
r = 0.5 cm
Frequency (GHz)
c
EMI SE$_T$ (dB)
ANF-MXene-PEDOT:PSS (60%)
ANF-MXene-PEDOT:PSS (50%)
ANF-MXene-PEDOT:PSS (40%)
PEDOT:PSS layer
MXene layer
ANF layer
10 μm
Frequency (GHz)
d
Electromagnetic shielding
Incident waves
Reflectd waves
Electromagnetic interface device
Multiple reflection and scattering
Transmitted waves
ANF
MXene nanosheets
PEDOT:PSS
e
R
A
T
X-band
Ku-band
K-band
Power efficiency
ANF film
ANF-MXene film
ANF-MXene-PEDOT:PSS (60%) film
f
EMI SSE$_t$ (dB·cm^2·g^{-1})
Thickness (mm)
MXene/CNF
MXene/TOCNFs
CNT/Cellulose
CNT/Rubber
Cu-Ni-CNT
CNT/PANI
CNT/WPU
CNT/Epoxy
CNT/Phenolic
PVA/RGO
PVA/MXene
PANI/SWCNTs
CNT/PP
This work
g1
15:03
85%
g2 ANF film
g3 ANF-MXene-PEDOT:PSS (60%) film
g4
15:05
h1
In charging
Ineffective electromagnetic shielding
ANF film
h2
Disable charging
Effective electromagnetic shielding
ANF-MXene-PEDOT:PSS (60%) film
In charging
Disable charging
Wireless charging
i
Average moisture permeability (0.48 g/d, ANF film)
Average moisture permeability (0.45 g/d, ANF-MXene-PEDOT:PSS(60%) film)
Average moisture permeability (0.47 g/d, ANF-MXene composite film)
Sample weight (g)
Days
j1
2-1
3-1
3-3
j2 ANF film
ANF-MXene composite film
ANF-MXene-PEDOT:PSS (60%) film

◂**Fig. 8** EMI shielding mechanism and moisture permeability of samples. **a** XRD patterns of ANF, ANF-MXene and ANF-MXene-PEDOT:PSS (60%) films after one month; **(b)** EMI shielding performances of ANF-MXene-PEDOT:PSS (60%) film after 10, 50 and 500 cycles of bending; **(c)** EMI shielding performances of ANF-MXene-PEDOT:PSS (40%), (50%) and (60%) films; **(d)** Related EMI shielding mechanism of ANF-MXene-PEDOT:PSS film; **(e)** Power efficiency of R, A and T of different films; **(f)** Comparison of EMI SSEt with the other materials (MXene/CNF [2], MXene/TOCNF [40], CNT/Cellulose [41], CNT/Rubber [42], Cu-Ni-CNT [43], CNT/PANI [44], CNT/WPU [45], CNT/Epoxy [46], CNT/Phenolic [47], PVA/RGO [3], PVA/MXene [32], PANI/SWCNTs [48], CNT/PP [49]); **(g-h)** Digital photograph and EMI shielding mechanism of ANF and ANF-MXene-PEDOT:PSS (60%) films for blocking wireless charging of the phone; **(i-j)** Moisture permeability testing of various films

the hybrid film of merely 0.2 g even withstood the weight of 500 g, which was 2500-fold loadings of own weight, further indicating light-weight and high-strength of films.

Related schematic diagram of fracture mechanism was exhibited in Fig. 4d. For ANF film, nanofilaments of 3D networks were pulled out, when subjected to external stresses (Fig. 4d). Accompanied by the deposition of MXene and PEDOT:PSS, MXene acted as an efficient glue, would induce the construction of high-density cross-linking networks to form a stable integrated structure and improve transfer efficiency of stress, thus alleviating the structural damage of film [36]. It also could be observed from Fig. 5a that the reconstruction of amide bonding and hydrogen bonding occurred simultaneously during hydrogel-induced ultra-fast protonation process. The above process would drive the construction of high-density hydrogen bonding networks by narrowing the molecular chain spacing. Compared with the method of vacuum filtration, the crosslinking networks of ANF film was denser and more uniform based on hydrogel induction. When subjected to external stretching, the molecular chains in ANF film would slip and hydrogen bonds between molecular chains were dislocated and reorganized, effectively avoiding the extension of cracks. The cross-sectional morphologies of films were recorded to further support the above explanation (Fig. 5b). It could be observed from Fig. 5b1 that the MXene layer exhibited a distinct laminated winkle structure. High aspect ratio nanofibers and MXene nanosheets were prone to forming mechanical interlocks on the interfacial region, resulting in a robust brick–mortar structure, which was in favor of stress diffusion along adjacent lamellar layers to reduce stress-concentrated zones (Fig. 5b2-3).

After folding, crimping and bending (Fig. 6a1-10), the ANF-MXene-PEDOT:PSS (60%) film still remained integrity and flatness without cracks and debris detachment, indicating excellent flexible properties. To further explore the adhesion of MXene and PEDOT:PSS layers, tape-peeling testing was conducted as shown in Fig. 6b1-b3. The surface of ANF-MXene and ANF-MXene-PEDOT:PSS (60%) films were tightly taped and peeled off separately after 30 s. For ANF-MXene film, partial MXene flakes retained on the tape and MXene layer was seriously damaged owing to the weak surface interaction (Fig. 6b3). For ANF-MXene-PEDOT:PSS (60%) film, few PEDOT:PSS and MXene nanofragments sticked on the tape, demonstrating that the existence of PEDOT:PSS enhanced the interaction between MXene and ANF to avoid the damage to functional layers (Fig. 6b3). Additionally, cross-section morphologies of ANF, ANF-MXene and ANF-MXene-PEDOT:PSS (60%) films were displayed in Fig. 6c1-3. The assembly of different functional layers was realized by the hydrogel-induced ultrafast protonation technology to further prepare high performance hybrid film (Fig. 6d1−6). This flexible, high-strength hybrid film demonstrated great application prospects in the aerospace and engineering machinery fields.

3.3 EMI shielding performance of ANF-MXene-PEDOT:PSS film

Electrical conductivity of films would directly affect the reflection and absorption of electromagnetic waves [38, 39]. Related testing results of ANF, MXene, PEDOT:PSS, ANF film, ANF-MXene film and ANF-MXene-PEDOT:PSS (60%) film were displayed in Fig. 7a. Regardless of non-conductive ANF and ANF film, the electrical conductivity of MXene, PEDOT:PSS, ANF-MXene film and ANF-MXene-PEDOT:PSS (60%) film reached 384.8, 1118.6, 37.0 and 264.7 S·cm^{-1}, respectively. Owing to the exceptional metal-like conductivity of MXene, the ANF-MXene film transformed from insulating into conductive. The rapid increase in the conductivity of ANF-MXene-PEDOT:PSS (60%) film could be attributed to the construction of abundant conductive pathways of 1D conductive polymers and 2D MXene nanosheets. As shown in Fig. 7c-d, the EMI SE$_T$ value of ANF film were all below 5 dB in X-band, Ku-band and K-band due to its insulating property, which was unable to meet commercial requirements of EMI shielding materials (≥ 20 dB) [2]. To improve the EMI shielding capacity of films, MXene with unique layered structure and high electrical conductivity was utilized to enhance the reflection of electromagnetic waves. It could be observed from Fig. 7d1-3 that the EMI SE$_T$ value of ANF-MXene film increased from 0.7 dB (ANF film) to 30.8–33.9 dB. Meanwhile, the EMI SE$_T$ value of ANF-MXene-PEDOT:PSS (60%) film reached 48.2, 45.7 and 47.8 dB, showing an increase of 6785.7%, 3164.3% and 4680.0% at X-band, Ku-band and K-band, respectively.

It could be seen in Fig. 7b that the shielding efficiency of ANF-MXene-PEDOT:PSS (60%) film was more than 99.99%. The above results further verified the influence of the increase in electrical conductivity on conduction loss and impedance mismatch [37]. Stability of EMI shielding

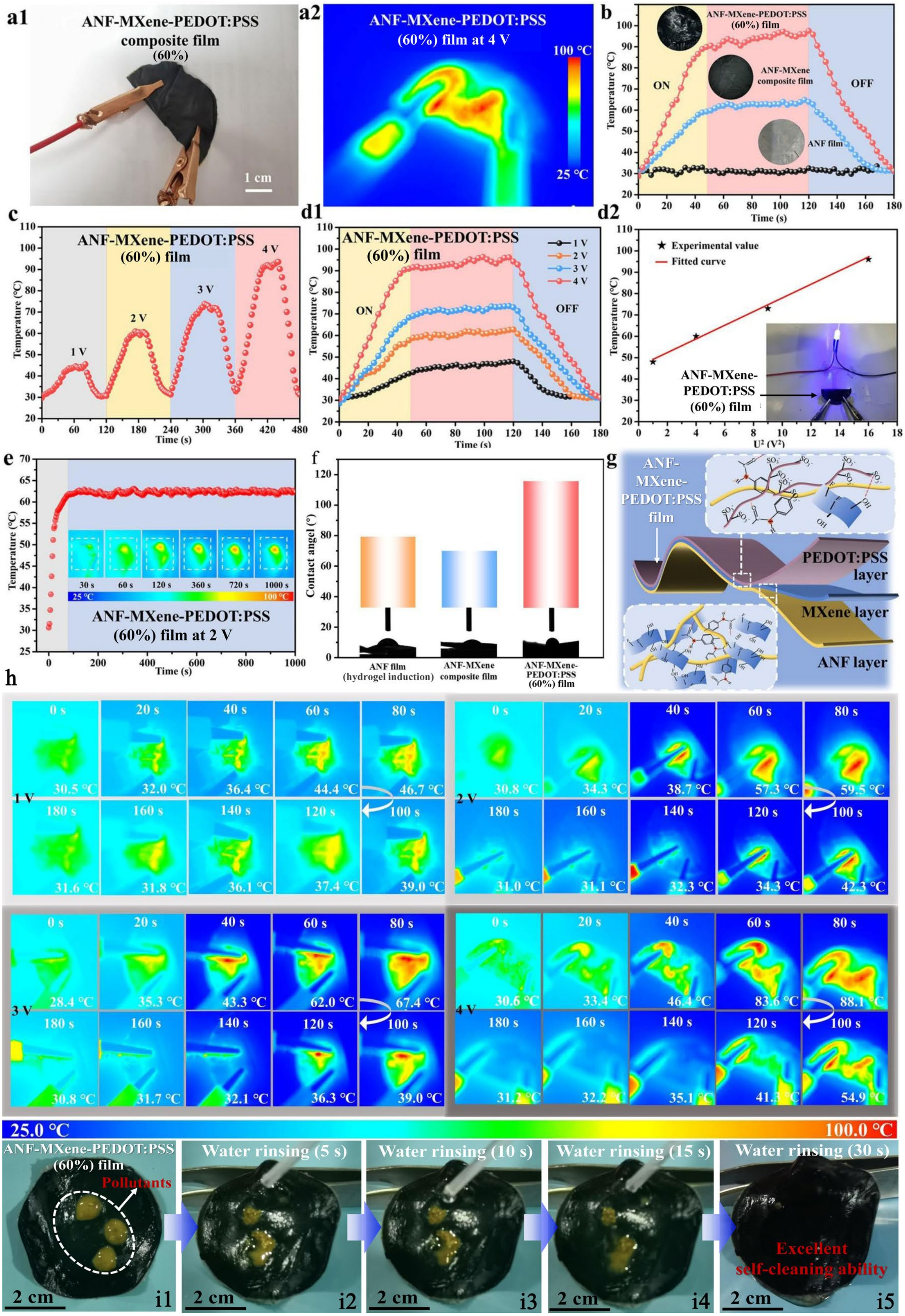
a1
ANF-MXene-PEDOT:PSS composite film (60%)
1 cm
a2
ANF-MXene-PEDOT:PSS (60%) film at 4 V
100 °C
25 °C
b
ANF-MXene-PEDOT:PSS (60%) film
ANF-MXene composite film
ANF film
ON
OFF
Temperature (°C)
Time (s)
c
ANF-MXene-PEDOT:PSS (60%) film
1 V
2 V
3 V
4 V
Temperature (°C)
Time (s)
d1
ANF-MXene-PEDOT:PSS (60%) film
1 V
2 V
3 V
4 V
ON
OFF
Temperature (°C)
Time (s)
d2
Experimental value
Fitted curve
ANF-MXene-PEDOT:PSS (60%) film
Temperature (°C)
U² (V²)
e
30 s
60 s
120 s
360 s
720 s
1000 s
25 °C
100 °C
ANF-MXene-PEDOT:PSS (60%) film at 2 V
Temperature (°C)
Time (s)
f
Contact angel (°)
ANF film (hydrogel induction)
ANF-MXene composite film
ANF-MXene-PEDOT:PSS (60%) film
g
ANF-MXene-PEDOT:PSS film
PEDOT:PSS layer
MXene layer
ANF layer
h
1 V
0 s 30.5 °C
20 s 32.0 °C
40 s 36.4 °C
60 s 44.4 °C
80 s 46.7 °C
100 s 39.0 °C
120 s 37.4 °C
140 s 36.1 °C
160 s 31.8 °C
180 s 31.6 °C
2 V
0 s 30.8 °C
20 s 34.3 °C
40 s 38.7 °C
60 s 57.3 °C
80 s 59.5 °C
100 s 42.3 °C
120 s 34.3 °C
140 s 32.3 °C
160 s 31.1 °C
180 s 31.0 °C
3 V
0 s 28.4 °C
20 s 35.3 °C
40 s 43.3 °C
60 s 62.0 °C
80 s 67.4 °C
100 s 39.0 °C
120 s 36.3 °C
140 s 32.1 °C
160 s 31.7 °C
180 s 30.8 °C
4 V
0 s 30.6 °C
20 s 33.4 °C
40 s 46.4 °C
60 s 83.6 °C
80 s 88.1 °C
100 s 54.9 °C
120 s 41.3 °C
140 s 35.1 °C
160 s 32.2 °C
180 s 31.2 °C
25.0 °C
100.0 °C
ANF-MXene-PEDOT:PSS (60%) film
Pollutants
Water rinsing (5 s)
Water rinsing (10 s)
Water rinsing (15 s)
Water rinsing (30 s)
Excellent self-cleaning ability
2 cm
i1
i2
i3
i4
i5

◂**Fig. 9** Joule heating properties of ANF-MXene-PEDOT:PSS film. **a1-a2** Digital photograph and infrared thermal image of ANF-MXene-PEDOT:PSS (60%) film; **(b)** Time–temperature curves of ANF, ANF-MXene and ANF-MXene-PEDOT:PSS (60%) films; **(c-d)** Time–temperature curves and U^2-temperature of ANF-MXene-PEDOT:PSS (60%) film at 1, 2, 3 and 4 V; **(e)** Time–temperature curves and infrared thermal images of ANF-MXene-PEDOT:PSS (60%) film at 2 V; **(f)** Contact angle of various films; **(g)** Schematic diagram of interfacial bonding of hybrid film; **(h)** Infrared thermal images of hybrid film at 1, 2, 3 and 4 V; **(i1-i5)** Self-cleaning experiment of ANF-MXene-PEDOT:PSS (60%) film

properties was also essential for EMI shielding materials. The EMI shielding properties of films were further tested after one month of exposure to air at room temperature as shown in Fig. 7e-f. It was obvious that the EMI SE_T value of ANF-MXene film decreased from 31.8–33.9 dB to 13.4–15.0 dB after one month (Fig. 7f1-3). Low chemical stability of MXene was highly susceptible to oxidization in air environments, resulting in the descend of conductivity and EMI shielding properties. The color of ANF-MXene film changed from black to gray and characteristic peaks of rutile and anatase titanium dioxide appeared in the XRD spectrum as shown in Fig. 8a, further illustrating the oxidation of MXene layer. For ANF-MXene-PEDOT:PSS (60%) film, the encapsulation of highly conductive PEDOT:PSS layer effectively slowed down the rapid oxidation of MXene layer. The above film still maintained relatively stable and high EMI shielding properties (43.8–46.0 dB) after one month during X-band, Ku-band and K-band (Fig. 7f1-3). It also could be observed from Fig. 8b that the EMI SE_T value of ANF-MXene-PEDOT:PSS (60%) film was still more than 44.5 dB after 500 cycles of bending, demonstrating its potential for application in EMI shielding of flexible electronic devices. Moreover, the EMI shielding performances of hybrid films with different loading of MXene-PEDOT:PSS were presented in Fig. 8c. With the loading increased from 40 *wt.%* to 60 *wt.%*, the EMI SE_T of hybrid film has risen from 37.8 dB to 48.2 dB (Fig. 8c). Constructing high-performance ANF-MXene-PEDOT:PSS film provided the possibility for solving the problems of air sensitivity and poor chemical stability of MXene-based hybrid materials.

To further explore the EMI shielding mechanism, related power efficiency of reflection (R), absorption (A) and transmission (T) of various films were displayed in Fig. 8e. For ANF-MXene and ANF-MXene-PEDOT:PSS (60%) films, the power efficiency of R was much higher than T and A at X-band, Ku-band and K-band. It could be observed that the value of R, A and T of ANF-MXene-PEDOT:PSS (60%) film reached 0.999, 0.001 and 0.000 (Fig. 8e). The above results indicated that the EMI shielding properties of ANF-MXene and ANF-MXene-PEDOT:PSS (60%) films were dominated by reflection. This could be ascribed to the impedance mismatch between the MXene/MXene-PEDOT:PSS layer and free space, which caused the reflection of most incoming microwaves before absorption [36]. Moreover, it could be seen in Fig. 8d that most microwaves were reflected when electromagnetic waves struck on the surface of ANF-MXene-PEDOT:PSS film due to impedance mismatch. With the penetration of remaining electromagnetic waves, ohmic losses and multiple internal reflections were conducive to dissipating the energy of surviving electromagnetic waves. Ultimately, multiple reflections between different layers in the film resulted in the minimal transmission of electromagnetic waves.

In order to eliminate the effects of thickness and density [19], the EMI SSE_t value was employed to comprehensively evaluate the EMI shielding performances of films. Differ from single-component conductive building blocks such as MXene and CNT as reported in the literatures [2, 40, 42–44, 50–53], dual-conducting hybrid networks of PEDOT:PSS and MXene demonstrated higher EMI shielding performances. Compared with other EMI shielding materials including MXene/CNF ($2647.0\ \mathrm{dB{\cdot}cm^2{\cdot}g^{-1}}$) [2], CNT/Rubber ($308.1\ \mathrm{dB{\cdot}cm^2{\cdot}g^{-1}}$) [42], PVA/RGO ($416.7\ \mathrm{dB{\cdot}cm^2{\cdot}g^{-1}}$) [3] et. al., the EMI SSE_t value of ANF-MXene-PEDOT:PSS (60%) film achieved $10{,}866.7\ \mathrm{dB{\cdot}cm^2{\cdot}g^{-1}}$ at 12.0 GHz (Fig. 8f). In this work, designing an ultra-thin ANF-MXene-PEDOT:PSS hybrid film with high-strength and excellent EMI shielding capacity exhibited strong competitiveness in the application of aerospace engineering fields. To further examine the EMI shielding capability of films in daily life, ANF and ANF-MXene-PEDOT:PSS (60%) films were placed between the phone and wireless charging device (Fig. 8g-h), respectively. It could be observed from Fig. 8g1-2 that the phone still could connect to the wireless charging device for charging despite the presence of ANF film. However, ANF-MXene-PEDOT:PSS (60%) film acted as a shielding barrier, which could effectively block the wireless charging signals for the phone (Fig. 8g3-4). The above results could be attributed to the high-efficiency EMI shielding capability of hybrid film, which contributed to reflection, absorption and multiple internal reflections of electromagnetic waves (Fig. 8h2). Additionally, the moisture permeability testing was carried out and related results were exhibited in Fig. 8i-j. Excellent breathability provided the possibility to prepare high-performance and comfort integrated hybrid films.

3.4 Joule heating properties of ANF-MXene-PEDOT:PSS film

As new-generation of EMI shielding materials, joule heating performance was also the focus of concern [54]. As displayed in Fig. 9a-h, the ANF-MXene-PEDOT:PSS (60%) film was cut into the circle with a diameter of 4 cm and folded in half to serve as an electric heater for testing joule heating capacity at 1, 2, 3 and 4 V. The above experiment followed the formula $Q = U^2/Rt$ (Q and U

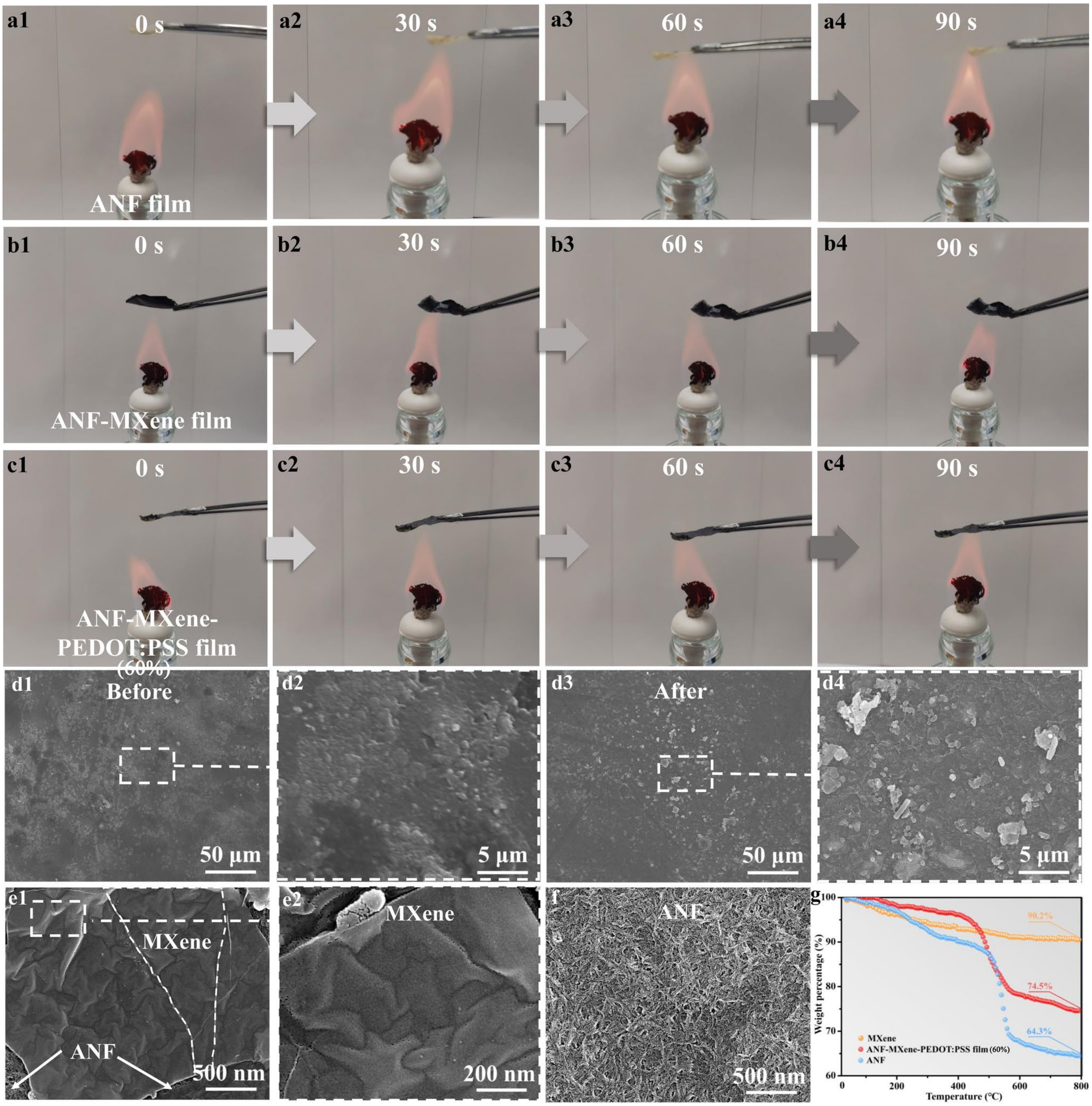

Fig. 10 Combustion experiments of various films**. a1-c4** Combustion experiments of ANF film, ANF-MXene film and ANF-MXene-PEDOT:PSS (60%) film for 90 s; **(d1-d4)** Surface morphologies of ANF-MXene-PEDOT:PSS (60%) film before and after combustion experiments; **(e1-e2)** SEM images of MXene and ANF in ANF-MXene-PEDOT:PSS (60%) film; **(f)** SEM images of ANF; **(g)** TG curves of various samples from 25 ℃ to 800 ℃

were generated heat and working voltage; R and t represented resistance and working time) [19]. It could be seen in Fig. 9b that the stable temperature of ANF-MXene-PEDOT:PSS (60%) film reached 94.3 ℃, compared with ANF film (31.5 ℃) and ANF-MXene film (61.2 ℃).

In addition, the temperature of hybrid film was stable at 45.3, 60.3, 71.1 and 94.3 ℃ after 50 s, under the voltage of 1, 2, 3 and 4 V (Fig. 9c-d1). Detailed infrared thermal images of ANF-MXene-PEDOT:PSS (60%) film were exhibited in Fig. 9h, from 0–180 s at 1, 2, 3 and 4 V. Achieving high temperature heating and instantaneous cooling in a short period of time were essential for an electrical heater. It was worth noting that the ANF-MXene-PEDOT:PSS (60%) film indicted an obvious linear relationship between temperature and U^2 (Fig. 9d2). Light-emitting diodes became brighter when the diode was connected in series with the ANF-MXene-PEDOT:PSS (60%) film, further illustrating good electrical conductivity of hybrid film. As displayed in Fig. 9e, ANF-MXene-PEDOT:PSS (60%) film worked at a voltage of 2 V for 1000 s, indicating the stability of long-term heating. Furthermore, it could be observed from Fig. 9f that the contact angles of ANF, ANF-MXene and ANF-MXene-PEDOT:PSS (60%) films were 79.4°, 70.0° and 115.8°, respectively. Owing to the conversion of surface hydrophilicity to hydrophobicity, ANF-MXene-PEDOT:PSS (60%) film exhibited excellent self-cleaning ability (Fig. 9i1-i5).

3.5 Fire-resistance and intelligent sensing of ANF-MXene-PEDOT:PSS film

To explore the fire-resistance properties of films, ANF, ANF-MXene and ANF-MXene-PEDOT:PSS (60%) films were placed on a burning alcohol lamp for 30, 60 and 90 s, respectively (Fig. 10a-c). It was obvious that ANF film shrank and crumpled when it exposed to fire (Fig. 10a1-4). However, ANF-MXene-PEDOT:PSS (60%) film still remained structural integrity and flatness after 90 s combustion testing, demonstrating certain flame-retardant performances (Fig. 10c1-c4).

Due to the oxidation effects from $Ti_3C_2T_x$ to TiO_2, the color of ANF-MXene film changed from black to grey. The coverage of PEDOT:PSS layer effectively protected the MXene layer from rapid oxidation, which kept black color of the film after long-time burning (Fig. 10d-f). Additionally, the residual weight of ANF, MXene and ANF-MXene-PEDOT:PSS (60%) film reached 64.3%, 90.2% and 74.5% at 800 ℃ (Fig. 10g), further displaying great thermal stability of hybrid film. Highly conductive ANF-MXene-PEDOT:PSS (60%) film was utilized as a strain sensor to realize the real-time monitoring of human pulsation, finger bending and weight pressure (Fig. 11a). The real-time monitoring process of human pulse signals and related testing results were shown in Fig. 11b and d. It was obvious that both folded and flat hybrid films in series with diodes exhibited excellent conductivity (Fig. 11c1-c5). Moreover, relative output voltage variation was detected at various finger bending angles (Fig. 11e). It could be observed from Fig. 11e that the degree of finger bending changed from 0° to 30°, 60° and 90°, which further generated a stable signal. The above process would result in a change in the relative resistance, further leading to the fluctuation of the output voltage. In addition, different weights (50, 100, 150, 200 and 300 g) were placed on the surface of the smart sensor to detect its sensitivity to external pressure (Fig. 11f-g). Due to high-strength, flexibility, high conductivity and strong EMI shielding capability, ANF-MXene-PEDOT:PSS film displayed great potential for the application in EMI shielding, thermal management and intelligent sensing fields (Fig. 11h-i).

4 Conclusions

In summary, nanoscale building blocks including 1D ANF, 2D MXene and 1D PEDOT:PSS were assembled to construct flexible and breathable ANF-MXene-PEDOT:PSS hybrid films according to a hydrogel-induced ultra-fast protonation process. Abundant conductive pathways and gradient laminar structures endowed the hybrid film with high conductivity and excellent EMI shielding properties. Compared with ANF film (0.7 dB), the EMI SE_T value of ANF-MXene-PEDOT:PSS (60%) film increased to 48.2 dB in the X-band. Meanwhile, the EMI SSE_t value of the hybrid film reached 10,866.7 $dB \cdot cm^2 \cdot g^{-1}$ at 12.0 GHz. After 500 cycles of bending, the EMI SE_T value of ANF-MXene-PEDOT:PSS (60%) film was still more than 44.5 dB. Additionally, superior joule heating properties guaranteed the temperature of hybrid film to rapidly heat and stabilize at 94.3 °C after 50 s. The high sensitivity and fast response of this film provided the possibility for real-time monitoring of human physiological signals. This work provided a direct path of assembling nanoscale building blocks to construct a multifunctional conductive film for the application in aerospace industry, electromagnetic protection and human–machine communication.

Author Contribution Writing and Manuscript Preparation (Shanshan Ma); Data Analysis and Interpretation (Jifeng Yan, Bin Ren, Hang Yu, Zhaoyang Ma and Lina Sun); Grammar Checking and Language Polishing (Siqi Liu, Jie Fei, Sanghoon Chae and Chaobin He); Experimental Work and Data Collection (Tengyang Zhang, Jinpeng Huo and Yuhui Yang); Conceptualization and Study Design (Shanshan Ma, Hejun Li and Jie Fei). All authors have checked and given approval to the manuscript.

Funding This research was supported by the National Natural Science Foundation of China (52172102), the National Research Foundation of Singapore, National University of Singapore, Agency for Science, Technology and Research (A*STAR), under its low carbon energy research (LCER) phase 2 HETFI Directed Hydrogen Project (U2307D4001), the National Key Research and Development Program of China (2023YFE0200700), the Key Scientific and Technological Innovation Research Team of Shaanxi Province (2022TD-31), the Key Research and Development Program of Shaanxi Province (2023GXLH-098) and the "Scientists + Engineers" Team of Shaanxi Province (2023KXJ-145).

Data availability No datasets were generated or analysed during the current study.

Declarations

Competing interests The authors declare no competing interests.

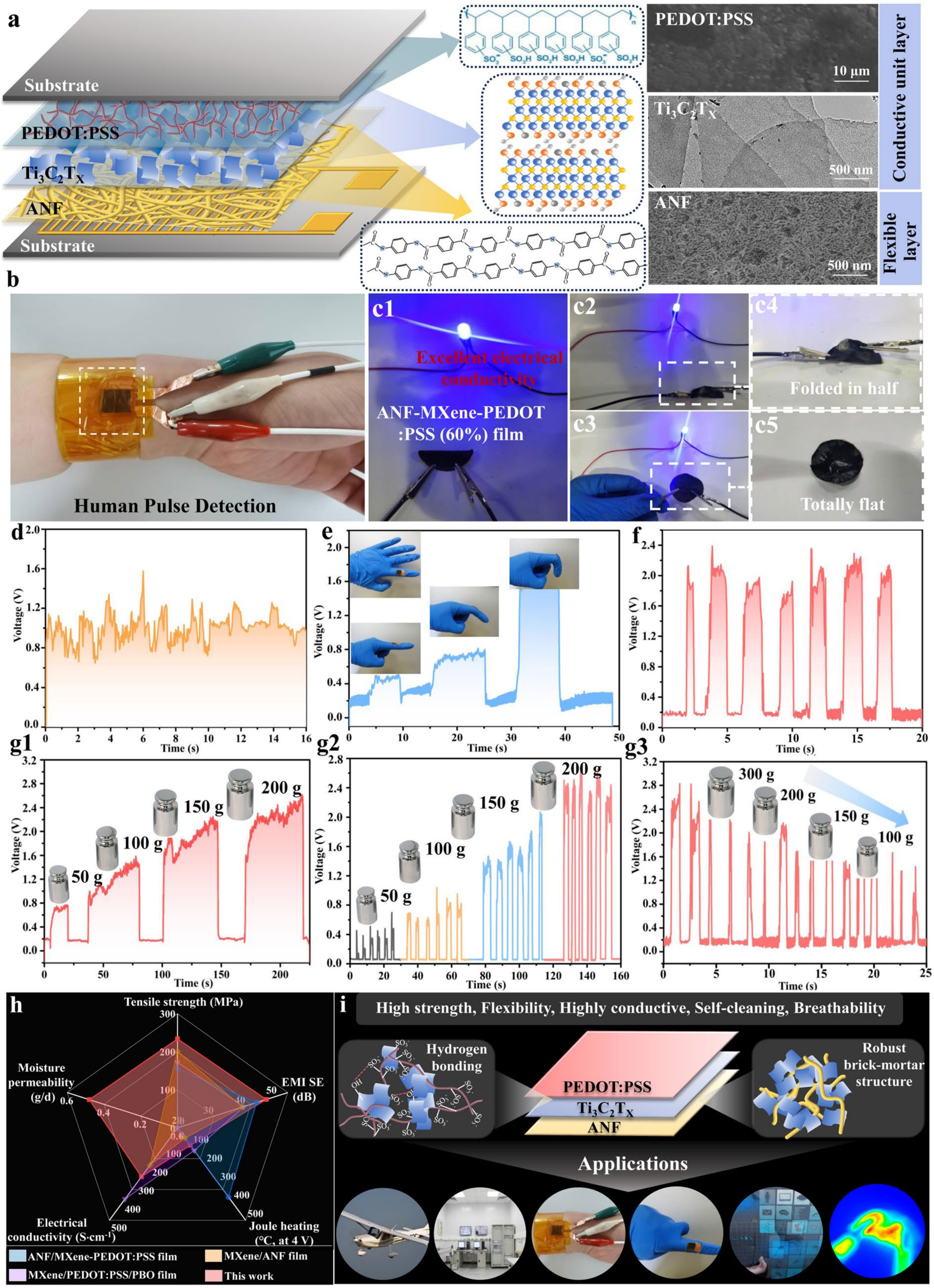
a
Substrate
PEDOT:PSS
$Ti_3C_2T_X$
ANF
Substrate
PEDOT:PSS
10 μm
$Ti_3C_2T_X$
500 nm
ANF
500 nm
Conductive unit layer
Flexible layer
b
Human Pulse Detection
c1
Excellent electrical conductivity
ANF-MXene-PEDOT:PSS (60%) film
c2
c3
c4
Folded in half
c5
Totally flat
d
Voltage (V)
Time (s)
e
Voltage (V)
Time (s)
f
Voltage (V)
Time (s)
g1
50 g
100 g
150 g
200 g
Voltage (V)
Time (s)
g2
50 g
100 g
150 g
200 g
Voltage (V)
Time (s)
g3
300 g
200 g
150 g
100 g
Voltage (V)
Time (s)
h
Tensile strength (MPa)
EMI SE (dB)
Joule heating (°C, at 4 V)
Electrical conductivity (S·cm⁻¹)
Moisture permeability (g/d)
ANF/MXene-PEDOT:PSS film
MXene/ANF film
MXene/PEDOT:PSS/PBO film
This work
i
High strength, Flexibility, Highly conductive, Self-cleaning, Breathability
Hydrogen bonding
PEDOT:PSS
$Ti_3C_2T_X$
ANF
Robust brick-mortar structure
Applications

◂**Fig. 11** Human physiological signal capturing and sensing of ANF-MXene-PEDOT:PSS (60%) film. **a** Diagram of ANF, MXene and PEDOT:PSS layers in ANF-MXene-PEDOT:PSS (60%) film; **(b, d)** Human pulse detection and related testing curve; **(c1-c5)** Electrical conductivity testing of ANF-MXene-PEDOT:PSS (60%) film; **(e)** Sensing test for finger bending at 30°, 60° and 90°; Related sensing curves under the pressure of **(f)** 150 g, **(g1-g2)** 50 g, 100 g, 150 g, 200 g and **(g3)** 100 g, 150 g, 200 g, 250 g; **(h)** Radar chart on the performance comparison with ANF/MXene-PEDOT:PSS [37], MXene/ANF [13] and MXene/PEDOT:PSS/PBO films [19]; **(i)** The wide application of ANF-MXene-PEDOT:PSS hybrid film

References

1. Wang M, Tian L, Zhang Q, You X, Yang J, Dong S (2023) Absorption-based electromagnetic interference shielding composites with sandwich structure by one-step electrodeposition method. Carbon 202:414–424. https://doi.org/10.1016/j.carbon.2022.10.090
2. Cao WT, Chen FF, Zhu YJ, Zhang YG, Jiang YY, Ma MG, Chen F (2018) Binary strengthening and toughening of MXene/cellulose nanofiber composite paper with nacre-inspired structure and superior electromagnetic interference shielding properties. ACS Nano 12(5):4583–4593. https://doi.org/10.1021/acsnano.8b00997
3. Araújo M, Carvalho A, Santos A, Padrón-Hernández E, Falcão E (2025) Influence of graphene oxide and reduced graphene oxide on TiO_2-reinforced flexible poly(vinyl alcohol) films for electromagnetic interference shielding. J Alloy Comp 1010:177671–177681. https://doi.org/10.1016/j.jallcom.2024.177671
4. Han Y, Ruan K, Gu J (2022) Janus (BNNS/ANF)-(AgNWs/ANF) thermal conductivity composite films with superior electromagnetic interference shielding and Joule heating performances. Nano Res 15(5):4747–4755. https://doi.org/10.1007/s12274-022-4159-z
5. Cao W, Ma C, Tan S, Ma M, Wan P, Chen F (2019) Ultrathin and flexible CNTs/MXene/cellulose nanofibrils composite paper for electromagnetic interference shielding. Nano-Micro Lett 11(1):72–89. https://doi.org/10.1007/s40820-019-0304-y
6. Shahzad F, Alhabeb M, Hatter C, Anasori B, Hong S, Koo C, Gogotsi Y (2016) Electromagnetic interference shielding with 2D transition metal carbides (MXenes). Science 353(6304):1137–1140. https://doi.org/10.1126/science.aag2421
7. Wang L, Ma Z, Zhang Y, Qiu H, Ruan K, Gu J (2022) Mechanically strong and folding-endurance $Ti_3C_2T_x$ MXene/PBO nanofiber films for efficient electromagnetic interference shielding and thermal management. Carbon Energy 4(2):200–210. https://doi.org/10.1002/cey2.174
8. Ma S, Zhang M, Nie J, Tan J, Song S, Luo Y (2019) Lightweight and porous cellulose-based foams with high loadings of zeolitic imidazolate frameworks-8 for adsorption applications. Carbohydr Polym 208:328–335. https://doi.org/10.1016/j.carbpol.2018.12.081
9. Ma S, Zhang M, Nie J, Tan J, Yang B, Song S (2019) Design of double-component metal-organic framework air filters with PM(2.5) capture, gas adsorption and antibacterial capacities. Carbohydr Polym 203:415–422. https://doi.org/10.1016/j.carbpol.2018.09.039
10. Ma S, Li H, Fei J, Huang Q (2024) Robust micro-nano hybrid aerogel derived from waste resources for thermal management and high-efficiency adsorption. Chem Eng J 486:150223–150238. https://doi.org/10.1016/j.cej.2024.150223
11. Yang B, Wang L, Zhang M, Luo J, Ding X (2019) Timesaving, high-efficiency approaches to fabricate aramid nanofibers. ACS Nano 13(7):7886–7897. https://doi.org/10.1021/acsnano.9b02258
12. Zhou Q, Lyu J, Wang G, Robertson M, Qiang Z, Sun B, Ye C, Zhu M (2021) Mechanically strong and multifunctional hybrid hydrogels with ultrahigh electrical conductivity. Adv Funct Mater 31(40):2104536–2104546. https://doi.org/10.1002/adfm.202104536
13. Weng C, Xing T, Jin H, Wang G, Dai Z, Pei Y, Liu L, Zhang Z (2020) Mechanically robust ANF/MXene composite films with tunable electromagnetic interference shielding performance. Compos Part A-Appl S 135:105927–105935. https://doi.org/10.1016/j.compositesa.2020.105927
14. Luo J, Zhang M, Nie J, Liu G, Tan J, Yang B, Song S, Zhao JR (2019) A deep insight into the structure and performance evolution of aramid nanofiber films induced by UV irradiation. Polym Degrad Stab 167:170–178. https://doi.org/10.1016/j.polymdegradstab.2019.07.001
15. Luo J, Zhang M, Yang B, Liu G, Tan J, Nie J, Song S (2019) A promising transparent and UV-shielding composite film prepared by aramid nanofibers and nanofibrillated cellulose. Carbohydr Polym 203:110–118. https://doi.org/10.1016/j.carbpol.2018.09.040
16. Ma S, Li H, Fei J, Li C (2023) Flexible-rigid scalable structures for trans-scale interface reinforcement of carbon fiber/phenolic composites: effect on properties. Compos Part B-Eng 258:110703–110716. https://doi.org/10.1016/j.compositesb.2023.110703
17. Ma S, Li H, Huang Q, Fei J (2023) Trans-scale interface engineering: constructing nature-inspired spider-web networks for regulating thermal transport and mechanical performance of carbon fiber/phenolic composites. J Colloid Interface Sci 653:777–794. https://doi.org/10.1016/j.jcis.2023.09.114
18. Zhou T, Yu Y, He B, Wang Z, Xiong T, Wang Z, Liu Y, Xin J, Qi M, Zhang H, Zhou X, Gao L, Cheng Q, Wei L (2022) Ultra-compact MXene fibers by continuous and controllable synergy of interfacial interactions and thermal drawing-induced stresses. Nat Commun 13(1):4564–4576. https://doi.org/10.1038/s41467-022-32361-6
19. Duan H, Wang C, Yi Y, Mu X, Ding H, Bi Z, Hu Y, Yu B (2024) Scalable, mechanically-robust, fire-resistance MXene/PEDOT:PSS/PBO film for efficient electromagnetic interference shielding and Joule heating performance. Chem Eng J 483:149302–149310. https://doi.org/10.1016/j.cej.2024.149302
20. Zhong Y, Lin Y, Yu H, Shao L, Cui X, Pang Q, Zhu Y, Hou R (2024) Construction methods and biomedical applications of PVA-based hydrogels. Front Chem 12:1376799–1376819. https://doi.org/10.3389/fchem.2024.1376799
21. Chen Y, Li J, Lu J, Ding M, Chen Y (2022) Synthesis and properties of poly(vinyl alcohol) hydrogels with high strength and

toughness. Polym Test 108:107516–107523. https://doi.org/10.1016/j.polymertesting.2022.107516

22. Han Z, Li D, Yang H, Zhao Y, Yin C, Yang K, Liu H, Sun W, Ling Z, Guan Q, Yu S (2022) Nacre-inspired nanocomposite films with enhanced mechanical and barrier properties by self-assembly of poly(lactic acid) coated mica nanosheets. Adv Funct Mater 32(32):2202221–2202229. https://doi.org/10.1002/adfm.202202221
23. Eichhorn V, Fatikow S, Sardan S, Hansen T, Bøggild M, Occhipinti L (2010) Novel four-point-probe design and nanorobotic dual endeffector strategy for electrical characterization of as-grown SWCNT bundles. IEEE International Conference on Robotics and Automation 6:4100–4105. https://doi.org/10.1109/ROBOT.2010.5509952
24. Li J, Wang Y, Ba D (2012) Characterization of semiconductor surface conductivity by using microscopic four-point probe technique. Phys Procedia 32:347–355. https://doi.org/10.1016/j.phpro.2012.03.568
25. Tontini G, Greaves M, Ghosh S, Bayram V, Barg S (2020) MXene-based 3D porous macrostructures for electrochemical energy storage. J Phys Mater 3(2):022001–022033. https://doi.org/10.1088/2515-7639/ab78f1
26. Han Y, Ruan K, He X, Tang Y, Guo H, Guo Y, Qiu H, Gu J (2024) Highly Thermally Conductive Aramid Nanofiber Composite Films with Synchronous Visible/Infrared Camouflages and Information Encryption. Angew Chem Int Ed Engl 63(17):202401538–202401544. https://doi.org/10.1002/anie.202401538
27. Xing H, He X, Wang Y, Zhang X, Li L, Wang Y, Cheng Z, Wu H, Ge Q, Li X (2023) Strong, tough, fatigue-resistant and 3D-printable hydrogel composites reinforced by aramid nanofibers. Mater Today 68:84–95. https://doi.org/10.1016/j.mattod.2023.07.020
28. Hu Y, Yang G, Zhou J, Li H, Shi L, Xu X, Cheng B, Zhuang X (2022) Proton donor-regulated mechanically robust aramid nanofiber aerogel membranes for high-temperature thermal insulation. ACS Nano 16(4):5984–5993. https://doi.org/10.1021/acsnano.1c11301
29. Ma S, Li H, Li C, Li B, Fei J, Wen Y (2022) Valuable aramid cellulose nanofibers derived from recycled resources for reinforcing carbon fiber/phenolic composites. Carbohydr Polym 292:119712–119725. https://doi.org/10.1016/j.carbpol.2022.119712
30. Wang X, Li S, Tu Y, Hu J, Huang Z, Lin S, Gui X (2021) Composite aramid membranes with high strength and pH-response. Polymers (Basel) 13(4):621–634. https://doi.org/10.3390/polym13040621
31. Tian W, Qiu T, Shi Y, He L, Tuo X (2017) The facile preparation of aramid insulation paper from the bottom-up nanofiber synthesis. Mater Lett 202:158–161. https://doi.org/10.1016/j.matlet.2017.04.127
32. Xu H, Yin X, Li X, Li M, Liang S, Zhang L, Cheng L (2019) Lightweight Ti_2CT_x MXene/poly(vinyl alcohol) composite foams for electromagnetic wave shielding with absorption-dominated feature. ACS Appl Mater Interfaces 11:10198–10207. https://doi.org/10.1021/acsami.8b21671
33. Yang B, Zhang M, Lu Z, Tan J, Luo J, Song S, Ding X, Wang L, Lu P, Zhang Q (2019) Comparative study of aramid nanofiber (ANF) and cellulose nanofiber (CNF). Carbohydr Polym 208:372–381. https://doi.org/10.1016/j.carbpol.2018.12.086
34. Yang B, Li W, Zhang M, Wang L, Ding X (2021) Recycling of high-value-added aramid nanofibers from waste aramid resources via a feasible and cost-effective approach. ACS Nano 15(4):7195–7207. https://doi.org/10.1021/acsnano.1c00463
35. Nie Z, Sun Y, Zhou T, Kong S, Liu L, Zhao C, Liu M (2023) Large-area ultrastrong and stiff aramid nanofiber based layered nanocomposite films. Nano Res 17(2):829–835. https://doi.org/10.1007/s12274-023-6123-y
36. Li W, Zhou T, Zhang Z, Li L, Lian W, Wang Y, Lu J, Yan J, Wang H, Wei L, Cheng Q (2024) Ultrastrong MXene film induced by sequential bridging with liquid metal. Science 385:62–68. https://doi.org/10.1126/science.ado4257
37. Zhou B, Song J, Wang B, Feng Y, Liu C, Shen C (2022) Robust double-layered ANF/MXene-PEDOT:PSS Janus films with excellent multi-source driven heating and electromagnetic interference shielding properties. Nano Res 15(10):9520–9530. https://doi.org/10.1007/s12274-022-4756-x
38. Ma X, Pan J, Guo H, Wang J, Zhang C, Han J, Lou Z, Ma C, Jiang S, Zhang K (2023) Ultrathin wood-derived conductive carbon composite film for electromagnetic shielding and electric heating management. Adv Funct Mater 33(16):2213431–2213439. https://doi.org/10.1002/adfm.202213431
39. Yao B, Hong W, Chen T, Han Z, Xu X, Hu R, Hao J, Li C, Li H, Perini S, Lanagan M, Zhang S, Wang Q, Wang H (2020) Highly Stretchable Polymer Composite with Strain-Enhanced Electromagnetic Interference Shielding Effectiveness. Adv Mater 32(14):1907499–1907505. https://doi.org/10.1002/adma.201907499
40. Zhan Z, Song Q, Zhou Z, Lu C (2019) Ultrastrong and conductive MXene/cellulose nanofiber films enhanced by hierarchical nano-architecture and interfacial interaction for flexible electromagnetic interference shielding. J Mater Chem C 7(32):9820–9829. https://doi.org/10.1039/c9tc03309b
41. Pang Z, Sun X, Wu X, Nie Y, Liu Z, Yue L (2015) Fabrication and application of carbon nanotubes/cellulose composite paper. Vacuum 122:135–142. https://doi.org/10.1016/j.vacuum.2015.09.020
42. Zhan Y, Oliviero M, Wang J, Sorrentino A, Buonocore G, Sorrentino L, Lavorgna M, Xia H, Iannace S (2019) Enhancing the EMI shielding of natural rubber-based supercritical CO_2 foams by exploiting their porous morphology and CNT segregated networks. Nanoscale 11(3):1011–1020. https://doi.org/10.1039/c8nr07351a
43. Ji K, Zhao H, Zhang J, Chen J, Dai Z (2014) Fabrication and electromagnetic interference shielding performance of open-cell foam of a Cu-Ni alloy integrated with CNTs. Appl Surf Sci 311:351–356. https://doi.org/10.1016/j.apsusc.2014.05.067
44. Saini P, Choudhary V, Singh B, Mathur R, Dhawan S (2009) Polyaniline-MWCNT nanocomposites for microwave absorption and EMI shielding. Mater Chem Phys 113(2–3):919–926. https://doi.org/10.1016/j.matchemphys.2008.08.065
45. Zeng Z, Chen M, Jin H, Li W, Xue X, Zhou L, Pei Y, Zhang H, Zhang Z (2016) Thin and flexible multi-walled carbon nanotube/waterborne polyurethane composites with high-performance electromagnetic interference shielding. Carbon 96:768–777. https://doi.org/10.1016/j.carbon.2015.10.004
46. Chen Y, Zhang H, Yang Y, Wang M, Cao A, Yu Z (2015) High-performance epoxy nanocomposites reinforced with three-dimensional carbon nanotube sponge for electromagnetic interference shielding. Adv Funct Mater 26(3):447–455. https://doi.org/10.1002/adfm.201503782
47. Teotia S, Singh B, Elizabeth I, Singh V, Ravikumar R, Singh A, Gopukumar S, Dhawan S, Srivastava A, Mathur R (2014) Multifunctional, robust, light-weight, free-standing MWCNT/phenolic composite paper as anodes for lithium ion batteries and EMI shielding material. RSC Adv 4(63):33168–33174. https://doi.org/10.1039/c4ra04183f
48. Raju P, Rani G, Kumar S, Joseph A, Raju K (2022) Ultrasonically induced in situ polymerization of PANI-SWCNT nanocomposites for electromagnetic shielding applications. J Mater Sci-Mater El 33(8):5138–5148. https://doi.org/10.1007/s10854-022-07702-2
49. Al-Saleh M, Sundararaj U (2009) Electromagnetic interference shielding mechanisms of CNT/polymer composites. Carbon 47(7):1738–1746. https://doi.org/10.1016/j.carbon.2009.02.030

50. Yuan B, Bao C, Qian X, Song L, Tai Q, Liew K, Hu Y (2014) Design of artificial nacre-like hybrid films as shielding to mitigate electromagnetic pollution. Carbon 75:178–189. https://doi.org/10.1016/j.carbon.2014.03.051
51. Zhao Y, Deng C, Yan B, Yang Q, Gu Y, Guo R, Lan J, Chen S (2023) One-step method for fabricating Janus aramid nanofiber/MXene nanocomposite films with improved Joule heating and thermal camouflage properties. ACS Appl Mater Interfaces 15(47):55150–55162. https://doi.org/10.1021/acsami.3c13722
52. Santos D, Queiroz J, Garcia I, Vieira J, Fernandes J, Sotgiu E, Minas G, Bouçanova M, Arruda L, Fangueiro R, Salgueiro-Oliveira A, Ainla A, Serra F, Dias R (2024) Flexible pressure and temperature microsensors for textile-integrated wearables. Actuators 13(1):42–57. https://doi.org/10.3390/act13010042
53. Zhang L, Yang B, Teng J, Lei J, Yan D, Zhong G, Li Z (2017) Tunable electromagnetic interference shielding effectiveness via multilayer assembly of regenerated cellulose as a supporting substrate and carbon nanotubes/polymer as a functional layer. J Mater Chem C 5(12):3130–3138. https://doi.org/10.1039/c6tc05516h
54. Wang Q, Zhang H, Liu J, Zhao S, Xie X, Liu L, Yang R, Koratkar N, Yu Z (2018) Multifunctional and Water-Resistant MXene-Decorated Polyester Textiles with Outstanding Electromagnetic Interference Shielding and Joule Heating Performances. Adv Funct Mater 29(7):1806819–1806828. https://doi.org/10.1002/adfm.201806819